2011

Distribution of Water Vapor in Molecular Clouds

G Melrick

V Tolls

Ronald L. Snell
University of Massachusetts - Amherst, snell@astro.umass.edu

E Bergin

D Hollenbach

See next page for additional authors

Authors

G Melrick, V Tolls, Ronald L. Snell, E Bergin, D Hollenbach, M Kaufman, D Li, and D Neufeld

Distribution of Water Vapor in Molecular Clouds

Gary J. Melnick, Volker Tolls

Harvard-Smithsonian Center for Astrophysics, 60 Garden Street, Cambridge, MA 02138

gmelnick@cfa.harvard.edu, vtolls@cfa.harvard.edu

Ronald L. Snell

Department of Astronomy, University of Massachusetts, Amherst, MA 01003

snell@astro.umass.edu

Edwin A. Bergin

Department of Astronomy, University of Michigan, 825 Dennison Building, Ann Arbor, MI 48109

ebergin@umich.edu

David J. Hollenbach

SETI Institute, 515 North Whisman Road, Mountain View, CA 94043

dhollenbach@seti.org

Michael J. Kaufman

Department of Physics and Astronomy, San Jose State University, One Washington Square, San Jose, CA 95192-0106

mkaufman@email.sjsu.edu

Di Li

Jet Propulsion Laboratory, 4800 Oak Grove Drive, Pasadena, CA 91109

dili@jpl.nasa.gov

and

David A. Neufeld

Department of Physics and Astronomy, Johns Hopkins University, 3400 North Charles Street, Baltimore, MD 21218

neufeld@pha.jhu.edu

ABSTRACT

We report the results of a large-area study of water vapor along the Orion Molecular Cloud ridge, the purpose of which was to determine the depth-dependent distribution of gas-phase water in dense molecular clouds. We find that the water vapor measured toward 77 spatial positions along the face-on Orion ridge, excluding positions surrounding the outflow associated with BN/KL and IRc2, display integrated intensities that correlate strongly with known cloud surface tracers such as CN, C_2H, ^{13}CO $J = 5-4$, and HCN, and less well with the volume tracer N_2H^+. Moreover, at total column densities corresponding to $A_V < 15$ mag., the ratio of H_2O to $C^{18}O$ integrated intensities shows a clear rise approaching the cloud surface. We show that this behavior cannot be accounted for by either optical depth or excitation effects, but suggests that gas-phase water abundances fall at large A_V. These results are important as they affect measures of the true water-vapor abundance in molecular clouds by highlighting the limitations of comparing measured water vapor column densities with such traditional cloud tracers as ^{13}CO or $C^{18}O$. These results also support cloud models that incorporate freeze-out of molecules as a critical component in determining the depth-dependent abundance of water vapor.

Subject headings: astrochemistry – ISM: abundances – ISM: clouds – ISM: molecules – radio lines: ISM

1. Introduction

Interstellar water is of continuing interest because of the role water plays in the oxygen chemistry within dense molecular clouds as well as the efforts to trace its abundance and distribution in all phases of cloud evolution through to planet formation. Thanks to a number of space-based observatories operated during the past 15 years, good progress has been made detecting and mapping the distribution of water toward molecular clouds. The highest water abundances, and the strongest water emission, are observed toward warm (i.e., $T > 300$ K) gas regions, most frequently associated with shock-heated gas generated by high-velocity outflows from young stellar objects and supernovae remnants. This finding is in agreement both with predictions that neutral-neutral reactions (i.e., $H_2 + O \rightarrow OH + H$ and $H_2 + OH \rightarrow H_2O$

+ H) dominate at these temperatures and are relatively efficient at producing water (cf. Elitzer & de Jong 1978; Elitzur & Watson 1978), and that non-dissociative shocks may be effective at liberating and heating water from ice mantles (Melnick et al. 2008). Observations suggest that typically between 1 and 20 percent of the elemental oxygen is driven into gas-phase H_2O via these processes (cf. Harwit et al. 1998; Melnick et al. 2000; Neufeld et al. 2000b; Nisini et al. 2000; Benedettini et al. 2002; Franklin et al. 2008).

However, within most dense ($n(H_2) > 10^3$ cm^{-3}) molecular cloud complexes, the bulk of the water – vapor plus ice – lies within the cooler ($T \lesssim 40$ K) and more massive quiescent gas component. Knowledge of the depth-dependent abundance of water vapor and water ice in molecular clouds is important for at least two reasons. First, the depth-dependent abundance of water vapor and water ice reflects a competition among a number of important processes, such as photodissociation, photodesorption, gas-phase reactions, gas-grain reactions, and grain-surface reactions, most of which depend upon the gas density and far-ultraviolet flux (FUV; 6 eV $< h\nu < 13.6$ eV). A better understanding of these processes and their relative importance thus reduces the uncertainty in virtually all models of the chemical composition of molecular clouds. Second, because oxygen is the most abundant element after hydrogen and helium, the processes that control the amount of oxygen locked in water vapor and, in particular, water ice determine the amount of residual oxygen free to react with other species. In this way, the predicted abundance of a host of species that depend on the gas-phase oxygen-to-carbon or oxygen-to-nitrogen ratio, for example, hinges on knowledge of the main reservoirs of oxygen, such as gas-phase water and water-ice.

Models incorporating the formation and destruction processes mentioned above have been constructed and detailed predictions exist for the water-vapor and water-ice abundance profiles as functions of cloud density and external FUV flux (cf. Hollenbach et al. 2009). Measures of the strength of solid-state H_2O absorption features along numerous lines of sight provide good column density distributions for water ice (e.g., Whittet et al. 1998; Sonnentrucker et al. 2008). Unfortunately, complementary studies of the distribution of gas-phase H_2O within quiescent molecular gas have suffered either from a lack of access to the ground-state ortho- and para-

water transitions, which probe most of the water column at $T < 40$ K, or from sparse spatial sampling of most clouds. In this paper we report the results from a large-area, fully-sampled study of ground-state water vapor emission toward the Orion Molecular Cloud ridge using the *Submillimeter Wave Astronomy Satellite* (*SWAS*).

The *SWAS* mission was primarily dedicated to the study of: (1) the oxygen chemistry in dense ($n(H_2) \gtrsim 10^3$ cm^{-3}) molecular clouds throughout our Galaxy; (2) the abundance, distribution, and cooling power of H_2O and O_2 within these clouds; and, (3) the structure and physical conditions in molecular clouds. To achieve these goals, *SWAS* was designed to detect emission from five key gas-phase atoms and molecules – water ($H_2^{16}O$)[1], isotopic water ($H_2^{18}O$), molecular oxygen (O_2), atomic carbon (CI), and isotopic carbon monoxide (^{13}CO). Since the emphasis was on studying the bulk of the colder ($T < 40$ K) molecular material, *SWAS* measured those frequencies coinciding with either the ground-state or a low-lying transition in each of these species. The one exception was ^{13}CO, for which the mid-level ($E_{upper}/k \simeq 79$ K) $J = 5 - 4$ transition was observed. Table 1 presents a summary of the species and transitions observed by *SWAS*. A detailed description of the *SWAS* mission can be found in Melnick et al. (2000b) and Tolls et al. (2004).

The Orion Molecular Cloud ridge is an approximately $10 - 15$ arcminute-wide region of warm ($T \sim 20 - 40$ K), dense ($n(H_2) \gtrsim 10^4 - 10^6$ cm^{-3}) gas (cf. Bally et al. 1987; Dutrey et al. 1991; Tatematsu et al. 1993; Bergin et al. 1994; Bergin, Snell, & Goldsmith 1996; Ungerechts et al. 1997; Johnstone & Bally 1999) stretching ~ 30 arcminutes north and more than 60 arcminutes south of BN/KL. As such, the Orion ridge represents the contiguous region with the largest angular size observed in water vapor by *SWAS* and provided the opportunity to obtain 86 independent spatial samples with *SWAS*'s 3.3×4.5 arcminute beam (at 557 GHz). Equally useful, as illustrated in Fig. 1, the Orion ridge presents a face-on geometry viewed from earth with its UV-illuminated surface on the near, earth-facing side. Thus, every line of sight probes a column of gas from its UV-illuminated surface to A_V's in excess of 30 magnitudes in some cases.

---

[1] Henceforth, the most abundant isotopologue of water, $H_2^{16}O$, will be denoted simply as H_2O.

Those species whose abundance peaks near the cloud surface would be expected to exhibit relatively little variation in the integrated intensity of their optically thin emission between lines of sight whose depth extends beyond the surface layers. Conversely, any optically thin emission from species whose abundance rises to a near-constant value throughout the cloud would be expected to scale with the line-of-sight column density. Thus, by measuring the correlation between the observed H_2O integrated intensities and the optically thin integrated intensities of both near-surface and volume-tracing species, it is possible to constrain the depth dependence of the water-vapor emission.

In §2 we review the *SWAS* and Five College Radio Astronomy Observatory (FCRAO) observations used in this study and, in §3, we present the results. In §4 we describe the role of line optical depth effects and depletion along with two approaches used to analyze the data. In §5 we discuss the results and implications for our understanding of the water distribution in dense molecular clouds.

2. Observations

The observations reported here were obtained with *SWAS* and the FCRAO 14-m telescope. *SWAS* utilized a 68×54-cm off-axis primary mirror coupled to two heterodyne receivers and a 1.4 GHz bandwidth acousto-optical spectrometer (AOS) backend. *SWAS* was able to observe either the O_2, CI, ^{13}CO, and H_2O, or the O_2, CI, and $H_2^{18}O$ lines simultaneously, and the AOS provided the equivalent of 210 km s^{-1} of baseline per spectral line. To ensure that the *SWAS* lines were centered in the AOS, regardless of the source v_{LSR} within the Galaxy, the receivers possessed a tuning range of ± 182 km s^{-1} at 490 GHz and ± 164 km s^{-1} at 553 GHz, in commandable steps of 7.3 and 6.6 km s^{-1}, respectively. The full-width-at-half-maximum (FWHM) for the *SWAS* beams were measured on orbit to be $3.'5 \times 5.'0$ at 490 GHz and $3.'3 \times 4.'5$ at 553 GHz, in good agreement with the predictions of diffraction theory for the *SWAS* telescope with an 11 dB Gaussian edge taper. Strip scans of Jupiter $\pm 10'$ across the beam minor axes and $\pm 12'$ across the beam major axes confirmed: (1) that the beams were symmetrical, with no

evidence for vignetting or other distortions; (2) that the beam centers were spatially co-aligned to within $5''$, or about 1/40 th of the FWHM of the minor axis of the 553 GHz beam; and, (3) the results of pre-launch instrument testing which showed that the highest sidelobe was suppressed by $\sim$ -17 dB with all other sidelobes below -30 dB out to $15'$ from the beam centers (the limit of these measurements).

The *SWAS* maps cover a grid of regular spacing of 3.2 arcminutes, corresponding approximately to the angular diameter of the minor axis of the *SWAS* beam at 557 GHz, the frequency of the othro-H_2O ground-state transition. All of the *SWAS* observations reported here were conducted by nodding the entire observatory. Because there was no change in the optical path between on-source and off-source reference observations, the spectral baselines were generally very flat, requiring no more than a first-order fit to the baseline to produce good-quality continuum-subtracted spectra. Spacecraft nodding also ensured that good reference positions were always used; spatial positions up to 3 degrees in any direction from the on-source position for each source were selectable and were chosen to coincide with the closest position exhibiting no detectable ^{12}CO $J = 1 - 0$ emission. On-orbit tests indicated that the receiver-AOS system was radiometrically very stable; measurements demonstrated that on-source integration times of ~ 200 hours continued to exhibit radiometric performance – i.e., spectral noise $\propto 1/\sqrt{\text{time}}$ – in both receivers. In addition, *SWAS* H_2O spectra of Orion BN/KL obtained 182 days apart were reproducible within the noise. The *SWAS* H_2O map of Orion was obtained during several periods of source availability between 20 December 1998 and 8 October 2003.

Between February and May 1999, the FCRAO 16-element SEQUOIA array receiver was used to obtain maps of the ^{12}CO and ^{13}CO emission (cf. Plume et al. 2000). Between January and June 2004, the FCRAO 32-pixel SEQUOIA array receiver (Erickson et al. 1999) was used to obtain maps of the emission from C_2H, HCN, N_2H^+, CH_3OH, $C^{18}O$ and CN. In April 2005, further observations were obtained in C_2H and N_2H^+ repeating regions in Orion where the emission was weak. The spectral lines observed by the FCRAO are summarized in Table 1. The region mapped in Orion covered the full spatial extent of the *SWAS* H_2O observations. For all observations, the data were obtained using an On-The-Fly observing technique. SEQUOIA has

the capability of observing two frequencies simultaneously which we utilized in mapping the six molecular species. The spectrometer for each pixel was a digital autocorrelator with a bandwidth of 50 MHz and 1024 spectral channels per pixel leading to a channel spacing that varied from 0.17 to 0.13 km s^{-1}, depending on the line frequency. The observations were first resampled to form maps with data spaced by 20$''$. The FWHM beam size of the FCRAO telescope varies from approximately 46$''$ at the CN line frequency to approximately 60$''$ at the C$_2$H line frequency. For the comparison with *SWAS* data, the FCRAO observations were further convolved with a Gaussian function to form spectra with a FWHM angular resolution of 3.9$'$, the geometric mean of two axes of the elongated *SWAS* beam at the H$_2$O line frequency, each centered on the locations of the *SWAS* observations and spaced by 3.2$'$. The main beam efficiency, η_{mb}, of the FCRAO antenna varies from approximately 0.45 (at 115 GHz) to 0.50 (at $\sim$ 100 GHz). The main beam efficiency for *SWAS* was 0.9.

The line profiles vary for different tracers and different sources. For example, in the center of Orion, there is a prominent outflow component that contributes significantly to the total intensity. There are also tracers with multiple hyperfine components, such as CN, C$_2$H, HCN, N$_2$H$^+$. To better recover the intensity of the relatively quiescent gas of interest here, one or more Gaussian components have been fitted to each spectrum. When multiple hyperfine components were present, the fitting was restricted by fixing: (1) the relative spacing between peaks to correspond to the known spectral separation between hyperfine components; and (2) the common linewidths of each component. For example, to fit the HCN emission, we allowed the LSR velocity of the main component to be a free parameter, v_0, and required that the other two components be centered at $v_0 - 7.064$ km s^{-1} and $v_0 + 4.842$ km s^{-1}, respectively, and that all components have the same linewidth. In this way, the hyperfine components were treated as correlated Gaussian peaks to best recover the total line flux.

3.   Results

The results of our mapping efforts are shown in Figs. 2 – 6. Fig. 2 shows a portion of the central ridge of the Orion Molecular Cloud traced by the 110.2 GHz ^{13}CO $J = 1$–0 transition. The irregularly-shaped area outlined in grey encompasses the region mapped in the 556.9 GHz 1_{10}–1_{01} ground-state ortho-H_2O transition by *SWAS*. The smaller grey square centered on ($\Delta\alpha$, $\Delta\delta$) = (0, 0) shows the area affected by the strong outflows from BN/KL and IRc2. Because the gas associated with the outflow shocks possesses temperatures, densities, and chemical abundances distinct from the surrounding quiescent material (cf. Blake et al. 1987), data from within this area are excluded from the following analysis. Fig. 3 shows the central region of the ridge mapped with $46''$ – $60''$ spatial resolution in six of the seven species observed using FCRAO (the 115.3 GHz ^{12}CO $J = 1$–0 map is not shown since its emission is optically thick within most of the area mapped by *SWAS*). As in Fig. 2, both the region mapped in H_2O by *SWAS* and the excluded shock-affected area are outlined.

Fig. 4 shows the *SWAS* 556.9 GHz 1_{10}-1_{01} ground-state H_2O integrated intensity map of the ridge along with the spectra upon which the map is based. Figs. 5 and 6 show the 492.2 GHz CI $^3P_1 - ^3P_0$ and 550.9 GHz ^{13}CO $J = 5$–4 integrated intensity maps of the ridge, respectively, also obtained using *SWAS*, as well as an expanded view of the area mapped deeply in H_2O.

A total of 86 spatial positions along the ridge were observed by *SWAS* with sufficient total integration times to either obtain convincing detections of H_2O emission or set meaningful upper limits to this emission. A considerably larger number of ridge positions were observed using *SWAS* for which the total integration times were less, but nonetheless sufficient to obtain good signal-to-noise spectra of the stronger CI and ^{13}CO $J = 5$–4 emission (Plume et al. 2000). These shorter-integration-time measurements were used to construct the extended (beyond the water-map) CI and ^{13}CO maps shown in Figs. 5 and 6. Thus, with the exclusion of the nine shock-affected lines of sight surrounding position (0,0), there remain 77 spatial positions for which integrated intensities were obtained for all species and which form the basis of the analysis of the quiescent gas. As noted in §2, the spatial grid of beam positions and the beam size –

synthesized in the case of the higher spatial resolution FCRAO maps – are the same for all species.

4.   Analysis

4.1.   *Line Optical Depth Effects*

H_2O: Optical depth effects can lead to an underestimate of the total water column density along a given line of sight, creating the appearance that water is a surface tracer when it is not. Such can be the case for water under certain restricted conditions (cf. Poelman, Spaans, & Tielens 2007). Is this the case here? The $1_{10}-1_{01}$ transition of $H_2^{16}O$ has a high critical density, $\sim 8 \times 10^7$ cm^{-3} at 30 K, and is expected to have a high optical depth for even a relatively low ortho-H_2O column density. Thus, line trapping plays an important role in the excitation of this transition. For large optical depths, the "effective critical density" is $A_{u\ell}/(C_{u\ell}\tau_o)$, where $A_{u\ell}$ is the spontaneous emission rate, $C_{u\ell}$ is the collisional de-excitation rate, and τ_o is the line-center optical depth. For densities less than the effective critical density, line photons may scatter multiple times but will eventually escape the cloud. In this limit, the line radiation is "effectively optically thin."

We examine the question of whether the observed H_2O lines toward the Orion ridge are effectively thin in two ways. First, we compute the emergent H_2O $1_{10}-1_{01}$ line flux for a set of densities and water abundances representative of the Orion ridge. These results are shown in Fig. 7. The line fluxes were computed under the large velocity gradient (LVG) approximation (see Neufeld & Melnick 1987, 1991); the collisional rate coefficients with o-H_2 and p-H_2 for the lowest 45 H_2O rotational energy levels, corresponding to a maximum upper-level temperature of ~ 2000 K, are those reported by Faure et al. (2007), the first five levels of which at 20 K are those reported by Dubernet et al. (2006). In order to bound the range of likely H_2 ortho-to-para ratios (OPR), which is presently unknown, results are given for the LTE OPR value at 30 K as well as an OPR value of 3. Among the 77 spatial positions considered here, the average measured H_2O line width is 3.9 km s^{-1}; we assume a line width of 3.5 km s^{-1} in our calculations. Finally,

we adopt a slab geometry which, because it yields the lowest escape probability for a given line-center optical depth, is the most conservative assumption; a polynomial fit to the exact expression for the photon escape probability from a plane-parallel emitting region (Hummer & Rybicki 1982) is used.

The maximum H_2O integrated antenna temperature, $\int T_A dv$, among the 77 positions considered is 3.26 K km s^{-1}. As can be seen in Fig. 7, for integrated intensities below the maximum observed, the line flux increases with column density very nearly linearly, as expected for optically thin emission; the deviation from linear behavior is less than 20 percent in all cases. Finally, similar analyses for gas temperatures of 20 K and 50 K (not shown) support the conclusion that the H_2O $1_{10}-1_{01}$ emission is effectively thin.

This result is consistent with that of Linke et al. (1977), who showed that if the main-beam antenna temperature, T_{mb}, satisfies $T_{mb} \ll (h\nu/4k)\exp(-h\nu/kT)$, then collisional excitation of the upper 1_{10} level always results in a photon that escapes the cloud. At a kinetic temperature, T, of 30 K, the H_2O 556.9 GHz line is effectively thin if $T_{mb} < 2.7$ K, or the antenna temperature is less than 2.5 K (for $\eta_{mb} = 0.9$). The peak observed antenna temperature for the H_2O emission from the Orion ridge is ~ 0.4 K, after correction for the *SWAS* main-beam efficiency. Thus, unless the beam filling factor for the H_2O emission is much less than 0.16, which appears unlikely given the distribution of gas shown in Figs. 2–6, the H_2O emission is effectively optically thin. Future H_2O 556.9 GHz mapping observations toward the Orion ridge using the *Herschel Space Observatory* should be able to further test this assumption.

^{13}CO: We are also interested in knowing whether the observed ^{13}CO emission provides a good measure of total cloud depth. To assess this, we compute the ^{13}CO column density required to achieve a line optical depth of 1 in the $J = 1-0$ transition using the RADEX LVG code (Van der Tak et al. 2007), the Einstein A-coefficients and collision cross-sections from the Leiden Atomic and Molecular Database (Schöier et al. 2005) for the lowest 40 rotational energy levels, and the assumption of no CO freeze-out. Line widths of 1.5 and 3 km s^{-1} are assumed; the average observed ^{13}CO $J = 1-0$ line FWHM is 2.8 km s^{-1}. As shown in Fig. 8, for a gas temperature of 30 K, the ^{13}CO $J = 1-0$ transition should be optically thin in most cases of

interest here. However, because a few lines of sight have a ^{13}CO line width less than 1.5 km s^{-1}, or may have a temperature less than 30 K, we choose to reference our measurements against the C^{18}O $J = 1 - 0$ transition to ensure a measure of the total cloud column density without concern for optical depth effects.

HCN, CN, C$_2$H, and N$_2$H$^+$: Several of the molecules observed have distinct hyperfine structure that can be used to estimate the optical depth of these lines. In the $J = 1 - 0$ transition of HCN, we observe the F=1-1, F=2-1 and F=0-1 hyperfine lines; in the $J = 1 - 0$ transition of N$_2$H$^+$, we observe the F$_1$=1-1, F$_1$=2-1 and F$_1$=0-0 hyperfine lines; in the $N = 1 - 0$, J=1/2-1/2 transition of C$_2$H, we observe the F=1-1 and F=0-1 hyperfine lines; and, in the $N = 1 - 0$, J=3/2-1/2 transition of CN, we observe the F=3/2-3/2, F=1/2-1/2, F=5/2-3/2 and F=3/2-1/2 hyperfine lines. If we assume that the hyperfine lines are populated according to LTE, we can use the observed hyperfine ratios to determine the optical depth in the strongest hyperfine component. The greatest leverage on the optical depth comes from the ratio of the strongest to the weakest hyperfine line; for spectra with good signal-to-noise ratios, relatively accurate optical depths can then be derived. For those HCN, CN, C$_2$H, and N$_2$H$^+$ spectra with good measures of all hyperfine components, we find that more than 90% of these spectra are consistent with line-center optical depths of less than 1 and, in no instance, was a line-center optical depth greater than 1.5.

4.2. *CO Depletion*

The C^{18}O integrated intensity can be used as a reliable measure of cloud depth only if CO remains undepleted throughout the column of gas observed. The gas-phase CO abundance is depleted mainly in two ways:

First, it is assumed that all CO that strike dust grains when the grain temperatures are $T_{\rm gr} \lesssim 20$ K will stick to the surface and be removed from the gas phase. The timescale for this process is $\sim 6 \times 10^4$ [5×10^3 cm^{-3}/n(H$_2$)] (30 K / T)$^{1/2}$ years (cf. Hollenbach et al. 2009), thus leading to the rapid freeze-out of CO unless subsequently desorbed.

Second, in regions where grain temperatures are above the sublimation temperature of CO-ice, but below that of H_2O-ice, i.e., $20\,\mathrm{K} < T_{\mathrm{gr}} < 90\,\mathrm{K}$, CO can still be depleted through reactions with He^+ and the continuous removal of elemental O from the gas-phase. Specifically, He^+ created by cosmic rays can react with CO to produce C^+, O, and He. The O thus produced can react to reform CO in the gas-phase or form H_2O in the gas-phase or on grain surfaces. Whether formed in the gas-phase or on grains, most of the H_2O will eventually end up on grain surfaces, where it will remain unless desorbed. In the absence of significant FUV photodesorption or cosmic-ray desorption, this process results in a steady decrease in the gas-phase elemental oxygen abundance and the significant depletion of CO in about 10^6 years.

It is well established that CO suffers strong depletion in the central parts of dense low-mass cloud cores, such as B68 (Bergin et al. 2006), L1544 (Caselli et al. 1999), L1498 (Willacy, Langer, & Velusamy 1998) IC 5146 (Kramer et al. 1999), and the Taurus molecular cloud (Pineda et al. 2010). Given the low dust temperatures measured toward the cores of these regions, it is assumed that direct CO freeze-out onto grains is primarily responsible for the observed depletion.

Is CO depletion significant within the Orion ridge? There are three reasons to believe that it is not a factor here. First, infrared and submillimeter observations toward the Orion ridge are best fit by dust temperatures between about 20 K and 30 K (e.g., Johnstone & Bally 1999; Mookerjea et al. 2000), making it unlikely that direct freeze-out of CO onto dust grains is occurring. Second, unlike in cold cores, Zinchenko, Caselli, & Pirogov (2009) find no evidence for CO depletion within other regions of high-mass star formation studied – i.e., W3, DR21, S140, S187, and S255. Third, the ratio of N_2H^+ to $C^{18}O$ integrated intensities toward the Orion ridge varies only by about a factor of two over the full range of observed $C^{18}O$ integrated intensities. Since negligible N_2H^+ depletion is observed toward colder regions of comparable density (see Tafalla et al. 2004, and references therein), particularly for depths into the cloud corresponding to the visual extinction range of greatest interest here, i.e., $A_V < 20$ (e.g., Bergin et al. 2002), the N_2H^+ to $C^{18}O$ ratio would be expected to increase by several orders of magnitude if CO depletion were significant. The absence of any substantial CO depletion may suggest that the

age of the Orion ridge is less than the timescale for CO depletion by He^+ destruction. Thus, throughout the remainder of this paper, we assume that CO is undepleted within the portion of the ridge observed in H_2O by *SWAS*.

4.3. *Abundance Profiles*

Because of the face-on appearance of the Orion ridge and its relatively strong extended emission, which permits many independent spatial samples, this source offers a particularly good opportunity to study observationally the distribution of water vapor in dense molecular clouds. To do so, we seek to examine correlations between gas-phase H_2O and a number of other species whose distribution with depth is believed to be well understood. With a face-on appearance, one method for investigating the line-of-sight distribution of a species is to plot its integrated intensity versus that of $C^{18}O$ (for the same spatial positions), where the optically thin $C^{18}O$ $J = 1 - 0$ emission serves as a proxy for the total column thickness of a given line of sight. Relating the $C^{18}O$ $J = 1 - 0$ integrated intensity to the total $C^{18}O$ column density, $N(C^{18}O)$, can be approached in two ways.

First, by assuming the $C^{18}O$ emission is optically thin and the background radiation terms can be ignored, it is possible to derive a simple analytical relation between the column density in the upper $J = 1$ state of the transition and the integrated intensity of the line (in K km s^{-1}), corrected by main-beam efficiency (~ 0.5 for FCRAO at the $C^{18}O$ line frequency):

$$N(J = 1) \ = \ 3.8 \times 10^{14} \ \times \ \int T_R(C^{18}O) \, dv \quad cm^{-2}, \tag{1}$$

where T_R is the radiation temperature ($= T_A^*$/main-beam efficiency).

Using a standard partition function, this gives the following expression for the total $C^{18}O$ column density:

$$N(C^{18}O) \ = \ 4.8 \times 10^{13} \, T/\left[e^{(-5.27/T)}\right] \ \times \ \int T_R(C^{18}O) \, dv \quad cm^{-2}, \tag{2}$$

where T is the gas temperature.

Second, using the LVG approximation, assuming an H_2 density of 10^5 cm^{-3}, and including all of the background radiation terms, we compute the C^{18}O integrated intensity for a range of column densities and temperatures. Fitting these data, we obtain the relation:

$$N(\text{C}^{18}\text{O}) \ = \ 1.9 \times 10^{14} \ T^{0.65} \ \times \ \int T_R(\text{C}^{18}\text{O})\, dv \quad \text{cm}^{-2}. \tag{3}$$

This expression is accurate for temperatures between 15 and 100 K and column densities where the emission is optically thin. As shown in Fig. 9, the two expressions are in good agreement, particularly over the range of temperatures most applicable to the Orion ridge – i.e., $20-40$ K (cf. Ungerechts et al. 1997). At $T = 30$ K, the optically thin criterion is satisfied if the maximum column density divided by line width (in km s^{-1}) is $N(\text{C}^{18}\text{O})/\Delta v \ < \ 3 \times 10^{16}$ s km^{-1} cm^{-2}. Since the measured C^{18}O $J = 1-0$ integrated intensities are all less than 4 K km s^{-1}, implying $N(\text{C}^{18}\text{O}) \lesssim 7 \times 10^{15}$ cm^{-2}, and the C^{18}O line widths are all greater than 0.95 km s^{-1}, the optically thin assumption is justified for the lines of sight considered here.

The relation between the C^{18}O and H_2 column densities is best established in dark clouds and is based on extinction determinations from the 2MASS data. For example, Kainulainen, Lehtinen, & Harju (2006) examine the ratio of $N(\text{C}^{18}\text{O})$ and A_V in Chamaeleon I and III-B using 2MASS and SEST data. Expressed in terms of the total visual extinction, A_V, averaging the two clouds presented in their paper yields approximately:

$$A_V \ = \ 5 \times 10^{-15} N(\text{C}^{18}\text{O}) \ + \ 2.3 \ = \ 0.95\, T^{0.65} \ \times \ \int T_R(\text{C}^{18}\text{O})\, dv \ + \ 2.3 \quad \text{mag}. \tag{4}$$

The offset is due to extinction of the surface layers where the gas-phase carbon is C$^+$ or CI, and not CO, and is uncertain and appears to vary from cloud to cloud (see summary by Harjunpää, Lehtinen, & Haikala 2004). Ignoring the offset, this relation leads to an abundance ratio of $N(\text{C}^{18}\text{O})/N(\text{H}_2) \sim 2 \times 10^{-7}$. The depth into the cloud, A_V, measured in visual magnitudes of extinction, as a function of C^{18}O integrated intensity for a range of assumed temperatures is

shown in Fig. 10. These results are in good agreement with the previous study of Lada et al. (1994).

Figs. 11 and 12 show plots of the ratio of the H$_2$O, C$_2$H, HCN, CN, CI, ^{13}CO $J = 1 - 0$, and N$_2$H$^+$ integrated intensities to those of C^{18}O $J = 1 - 0$ as a function of the C^{18}O $J = 1 - 0$ integrated intensity. The corresponding depth into the cloud, in visual magnitudes, is shown along the top axis of each plot. For these values, Eqn. (4) is used assuming $T = 30$ K. For the near-surface depths of particular interest here, corresponding to C^{18}O integrated intensities less than about 1.5 K km s^{-1}, the A_V derived from the C^{18}O intensity is relatively insensitive to the assumed temperature.

Because the emission from most species toward BN/KL is strongly affected by the outflow, the data corresponding to the $(\Delta\alpha, \Delta\delta) = (0, 0)$ and surrounding 8 positions are not included in these plots. To better reveal any trends (by reducing the scatter in the 77 data points), the ratio values have been co-averaged in bins of C^{18}O $J = 1$-0 integrated intensity of width 0.2 K km s^{-1} in the x-axis. The plotted y-value within each bin is the weighted mean, $\mu = \Sigma(y_i/\sigma_i^2)/\Sigma(1/\sigma_i^2)$, of the i data points lying within that bin, where y_i is the ratio of the integrated intensity, I, of species a to species b for point i, i.e., $y_i = I_{a,i}/I_{b,i}$, and $\sigma_i = \left[y_i^2 \left(\sigma_{a,i}^2/I_{a,i}^2 + \sigma_{b,i}^2/I_{b,i}^2\right)\right]^{1/2}$, where $\sigma_{a,i}$ and $\sigma_{b,i}$ are the 1σ uncertainties associated with the i-th integrated intensity for species a and b, respectively. The 1σ y-value error bars represent the uncertainty of the mean, $\sigma_\mu = \left[1/\Sigma(1/\sigma_i^2)\right]^{1/2}$. Though barely visible in these plots, the 1σ error bars representing the x-value dispersion within each bin are also shown.

The results fall broadly into two categories – i.e., those species that exhibit an increase in their integrated intensities relative to C^{18}O toward lower A_V's and one that shows an increase in this ratio with depth. Specifically, C$_2$H, CN, HCN, and CI all show a steady rise in the observed intensity ratio toward the cloud surface, with the possible indication that the CN and HCN profiles subsequently decrease at $A_V < 5$. Conversely, the ratio of N$_2$H$^+$ to C^{18}O integrated intensities appears to increase with depth.

One measure of whether these plots convey an accurate picture of the abundance profiles

is provided by the observed profile of ^{13}CO/C^{18}O integrated intensities, shown in Fig. 12. Assuming the observed ^{13}CO $J = 1 - 0$ line is optically thin and depletion of CO is not significant along the ridge, the ^{13}CO/C^{18}O intensity ratio deep in the cloud is expected to reflect the isotopic ratio of ^{16}O/^{18}O of 500 and ^{12}C/^{13}C of between 43 (Hawkins & Jura 1987; Stacey et al. 1993; Savage et al. 2002) and 65 (Langer & Penzias 1990), i.e., ^{13}CO/C^{18}O $\simeq$ 8-12. The observed ^{13}CO/C^{18}O intensity ratio deep in the cloud is in good agreement with these values and, thus, provides reason to believe the inferred profiles are descriptive of the actual profiles.

Fig. 11 clearly shows an increase in the H_2O/C^{18}O intensity ratio at $A_V < 15$, with a steady rise toward the cloud surface. Because the increase is evident between $A_V \sim 5$ and 15, where the C^{18}O abundance is predicted to be approximately constant, the inferred increase in the H_2O emission toward the cloud surface appears to be real.

4.4. *Principal Component Analysis*

A second method for studying the correlations between species involves use of multivariate analysis referred to as Principal Component Analysis (PCA). PCA's goal is to find, among linear combinations of the data variables, a sequence of orthogonal, or completely uncorrelated, factors that most efficiently explain the differences in the data. Details of this method are provided elsewhere (cf. Ungerechts et al. 1997, for applications to astronomical mapping data) and will not be repeated here, except to note that the PCA approach provides a useful and compact means for quantifying the commonality between maps made in different transitions.

In PCA, we attempt to explain the total variability of p correlated variables through the use of p orthogonal principal components (PC). The components themselves are merely weighted linear combinations of the original variables such that PC 1 accounts for the maximum variance in the data of any possible linear combination, PC 2 accounts for the maximum amount of variance not explained by PC 1 and that it is orthogonal to PC 1, and so on. Even though use of all p PC's permits the full reconstruction of the original data, in many cases the first few PC's are sufficient to capture most of the variance in the data. Thus, we can express each observed map (to within the noise) as a different linear combination of just two or three maps (i.e. two or

three principal components).

To ensure that the analysis gives equal weighting to each line – versus allowing the brightest lines to dominate the analysis – the integrated intensities for each spectral line have been mean subtracted and divided by the standard deviation. In addition, to reduce the variance due to excitation and varying line emissivity, only those transitions with a critical density greater than 10^4 cm^{-3} (see Table 1) are included in the PCA. The results are shown in Fig. 13.

The interpretation of these results is straightforward. The top panel in Fig. 13 plots the fraction of the total variance in the data captured by each principal component. For the data considered here, 90% of the total variance between species is accounted for with principal components one and two, and 96% of the total variance is accounted for with the addition of principal component three.

The lower two panels in Fig. 13 plot the coefficients for the first and second, and second and third, principal components, respectively. Because almost all of the variation in the data is in principal components one and two, the bottom left panel is most relevant. There are two key elements in the plot to note: (1) the degree to which each vector approaches the unit circle; and, (2) the clustering of vectors. Because the principal components are normalized such that the quadrature sum of the coefficients for each species is unity, the proximity of the points to the circle of unit radius is a measure of the degree to which any two principal components account for the total variance in this sample. Consequently, the closeness of all the points to the unit circle in the lower left panel is a reflection of the fact that these two principal components contain almost all of the variance in the data, as noted above.

The degree of clustering of the vectors is a measure of their correlation. As noted by Neufeld et al. (2007), in the limit where two points actually lie on the unit circle, the cosine of the angle between these points is their linear correlation. Thus, points that coincide on the unit circle (i.e., $\Delta\theta = 0°$) would indicate perfectly correlated data, whereas points on opposite sides of the circle (i.e., $\Delta\theta = 180°$) would indicate perfectly anticorrelated data. Thus, the plot of PC1 versus PC2 quantifies what appears evident in Figs. 11 and 12, namely that the ground-

state ortho-H_2O emission is well correlated with the CN, HCN, and C_2H emission. The H_2O emission is also well correlated with the ^{13}CO $J = 5$–4 emission. Since the upper level of this ^{13}CO transition is 79 K above the ground state, it too is expected to trace the warmer surface layers of the ridge. The vectors representing H_2O and N_2H^+ in this plot show the greatest separation, suggesting no particular correlation exists between the lines of sight where the H_2O and N_2H^+ integrated intensities are strong.

The bottom right panel in Fig. 13, i.e., PC2 versus PC3, shows the distribution of residual variance between the species. The short vectors (from the 0,0 point) illustrate quantitatively the relative unimportance of additional sources of variance between species beyond those captured in the first two principal components.

5. Discussion

The distribution of water vapor within a molecular cloud depends upon both the gas-phase chemistry that forms H_2O and a number of important micro-physics processes. These processes include the rate at which oxygen atoms strike dust grains and combine with hydrogen on their surfaces to form OH and H_2O, the rate at which such H_2O is removed from grain surfaces by incident UV photons (i.e., photodesorption) and cosmic rays, and the rate at which gas-phase H_2O is destroyed by UV photons (i.e., photodissociation). Because these processes are operative in all quiescent molecular clouds to varying degrees, testing models that incorporate the necessary chemistry and physics is important. Water is a particularly good diagnostic since its gas-phase abundance is sensitive to all of the above processes. In addition, water is a molecule of great (and growing) inherent interest.

The need to refine our understanding of water vapor in molecular clouds, and the motivation for this study, results from two main *SWAS* findings. First, it became clear early in the *SWAS* mission that more than just gas-phase chemical models are needed to explain the inferred H_2O abundances toward quiescent clouds. In particular, in cold ($T \lesssim 30$ K), dense ($n(H_2) \gtrsim 10^4$ cm^{-3}) clouds, the inferred abundance of gaseous H_2O is ~ 100 to 1000 times less than the predic-

tions of ion-neutral gas-phase chemical models and the O_2 abundance is at least 100 times less than predictions (cf. Neufeld, Lepp, & Melnick 1995; Snell et al. 2000c; Goldsmith et al. 2000; Bergin et al. 2000; Melnick 2004).

A post-flight review of the *SWAS* data revealed a second important clue. As shown in Fig. 14, the peak antenna temperatures observed toward 83 giant and dark cloud cores display a relatively small spread in values; almost 70 percent of the sources observed have a peak antenna temperature within a factor of two of 100 mK. To understand why this is significant, it is useful to consider how the line emission scales with the physical conditions. For effectively thin emission, the $1_{10}-1_{01}$ 556.9 GHz integrated intensity can be expressed as

$$\int T_A\, dv = \eta_{\mathrm{mb}}\, C_{u\ell} \left(\frac{h\nu}{4\pi}\right) \left(\frac{c^3}{2k\nu^3}\right) x(\mathrm{o}-\mathrm{H_2O})\, N(\mathrm{H_2})\, n(\mathrm{H_2})\, e^{-h\nu/kT_K} \quad \mathrm{K\ km\ s^{-1}}, \quad (5)$$

where ν is the line frequency, $x(\mathrm{o–H_2O})$ is the ortho-H_2O abundance (relative to H_2), $N(\mathrm{H_2})$ is the H_2 column density, and $n(\mathrm{H_2})$ is the H_2 volume density. Consequently, in the optically thin limit, the integrated intensity increases linearly with increasing H_2 column and volume densities, even if the line center optical depth is large. Since the measured velocity-resolved line widths (FWHM) toward quiescent giant and dark clouds are all within a factor of two of 5 km s^{-1}, the peak antenna temperatures should reflect the spread in $x(\mathrm{o–H_2O})$, $N(\mathrm{H_2})$, and $n(\mathrm{H_2})$ among the sources.

The relatively small variation in the peak H_2O line intensity between sources with more than order-of-magnitude differences in H_2 column densities (inferred from both ^{13}CO and $C^{18}O$ measurements), and H_2 volume densities (inferred from a variety of molecular species) suggests that the ortho-water column density, i.e., $x(\mathrm{o–H_2O})\, N(\mathrm{H_2})$, and H_2 density within the water-emitting region are not particularly sensitive to the total depth and peak density of the target clouds. Such could only be the case if the water-vapor emission originates predominantly from a zone within the cloud whose density, column density, and H_2O abundance are tightly coupled, with little variation from cloud to cloud.

Ideally, it would be desirable to directly measure the depth dependence of the water emission. Regrettably, this is impossible with the face-on appearance of the Orion ridge and attempts to do so indirectly – for example, by modeling the emission from each of the 77 lines of sight considered here – are complicated by often unknown variations in the physical conditions along the ridge, including the varying incident FUV flux. Instead, we seek to extract the desired information from the ensemble of data, such as whether the water-vapor emission correlates better with surface tracers (i.e., species whose depth of peak abundance is relatively small and located near the cloud surface), or volume tracers (i.e., species whose abundance increases and attains a near-constant maximum with depth into the cloud).

Models of PDR's provide the detailed predictions necessary to identify the surface and volume tracers. Unfortunately, the depth-dependent abundance profiles are affected by the strength of the incident FUV field, which varies along the Orion ridge. Stacey et al. (1993) have modeled the FUV-sensitive $157.74\,\mu$m [C II] emission from OMC-1 and find that the value of G_{o}, the factor by which the FUV field exceeds the local interstellar value, at d parsecs projected distance, or θ_{sep} arcminutes angular separation, between the Trapezium cluster and a given point along the ridge is given by

$$G_{\mathrm{o}} = \frac{8.6 \times\ 10^3}{(d^{\,2} + d_c^2)^{1.5}} = \frac{8.6 \times\ 10^3}{\left([480\tan(\theta_{\mathrm{sep}}/60)]^2 + 0.152\right)^{1.5}}\ ,\qquad (6)$$

where d_c is the distance, in parsecs, along the line of sight between the foreground Trapezium cluster and the molecular cloud, assumed to be 0.39 pc (see Fig. 1). Thus, for the ridge positions considered here, G_{o} is expected to vary between $\sim 2 \times 10^4$ and ~ 100 from about 5 to 30 arcminutes from BN/KL, respectively. The presence of a large number of B-stars in the Orion molecular cloud complex, in addition to the OB stars in the Trapezium cluster, suggests that the strength of the FUV field predicted by Eqn. (6) far from BN/KL is likely to be a lower limit.

Fig. 15 shows the predicted depth-dependent gas-phase abundance profiles for the observed species for $100 \leq G_{\mathrm{o}} \leq 2 \times 10^3$, while Fig. 16 shows the predicted profiles for $10^4 \leq G_{\mathrm{o}} \leq 2 \times 10^5$.

It is important to note that these models assume that H_2O remains in the gas phase throughout the cloud and does *not* freeze out. As discussed earlier, the freeze out of H_2O locks elemental oxygen in ice, reducing the gas-phase oxygen abundance and altering the gas-phase chemistry. If this is the case, as the current data suggest, then the abundance profiles in Figs. 15 and 16 no longer reflect the actual abundance profiles at depths greater than $A_V \sim 6-8$ where H_2O begins to freeze out for the densities and G_o's relevant to the Orion ridge (see Hollenbach et al. 2009). Nevertheless, the H_2O freeze-out point lies beyond the depth where all but two of the species observed here – i.e., CO and N_2H^+ – peak and, thus, these figures provide some guidance. (As discussed in §4.2, it is assumed that CO and N_2H^+ are undepleted within the region of interest here.)

Over the broad range of FUV field strengths relevant here, species such as C, CN, C_2H, and HCN are predicted to reach their peak abundance within 8 visual magnitudes of the cloud surface and subsequently decrease in abundance. Though observations of CI provide some evidence for emission in molecular cloud interiors (e.g., Keene et al. 1985), its creation via CO photodissociation clearly establishes this species as a surface tracer. C_2H and CN have been found to trace the edges of clouds exposed to UV radiation (Jansen et al. 1995b; Rodríguez-Franco et al. 1998). In general, these simple carbon-based radicals can form rapidly via reactions between C and C^+ with other simple molecules (e.g., Sternberg & Dalgarno 1995). This will lead CN and C_2H to trace regions where CI and C^+ are abundant (e.g. the cloud surface). The formation of HCN is more complex, with several contributing pathways, but in general this species can form in abundance in regions where CI/CO ~ 1, and thus it too can appear in abundance at low to moderate extinctions where CI is present.

Alternately, species such as ^{12}CO, ^{13}CO, $C^{18}O$, and N_2H^+ rise in abundance between 2 and 8 visual magnitudes of the surface and maintain near-constant values with increasing depth. In the case of N_2H^+, this molecule requires the *a priori* formation of N_2, which itself forms in a staged process through $N + OH \rightarrow NO + H$ and $NO + N \rightarrow N_2 + O$. These neutral-neutral reactions are not fast enough to compensate for photodissociation, leading N_2H^+ to preferentially appear in abundance only at greater depths.

For CI, CN, HCN, C_2H, ^{13}CO and N_2H^+, the trends indicated in the models are reflected in the observed profiles shown in Figs. 11 and 12. Because the $C^{18}O$ abundance is predicted to decrease sharply for $A_V < 5$ (due to FUV photodestruction of the molecule), it's useful to restrict our consideration to $A_V \gtrsim 5$ where the $C^{18}O$ abundance is predicted to be relatively constant. Specifically, C_2H, CN, and CI, all of which have their predicted peak abundance at $A_V < 4$ over the full range of G_o, show a steady rise in the observed intensity ratio toward the cloud surface. Likewise, HCN, which is predicted to peak in its abundance at $A_V \simeq 6-7$, shows an increase in the measured $HCN/C^{18}O$ intensity ratio toward these A_V's, with perhaps an indication that the HCN abundance may yet be higher than predicted at $A_V \sim 5$. Conversely, N_2H^+, which is predicted to achieve a near-constant abundance at $A_V \gtrsim 9$, if anything shows a slightly increasing $N_2H^+/C^{18}O$ intensity ratio beyond an A_V of ~ 25. Within a number of other high-mass clouds, the N_2H^+ abundance is observed to increase in regions of lower fractional ionization due to decreased rates of dissociative recombination (Zinchenko, Caselli, & Pirogov 2009). This may also explain the rise in the $N_2H^+/C^{18}O$ intensity ratio toward higher A_V's observed in Orion.

However, the observed H_2O profile is in conspicuous disagreement with the predictions of the PDR models summarized in Figs. 15 and 16. These models, which neglect H_2O freeze-out, predict a steady increase in the gas-phase water abundance between an $A_V \sim 2$ and 10, reaching a steady-state abundance of $\sim 2\times10^{-5}$. In addition to predicting a gas-phase H_2O abundance more than two orders of magnitude greater than observed, the predicted H_2O abundance profile would lead to a tighter correlation with N_2H^+, and a reduced correlation with ^{13}CO $J = 5-4$, CN, HCN, and C_2H, than indicated by the principal component analysis.

It is worth asking whether the correlation between the H_2O emission and the other surface tracers reflects little more than the preferential excitation of water vapor in the warmer surface layers? To examine this possibility we consider three cases shown in Fig. 17. First, we compute the depth-dependent H_2O emission resulting from the PDR models of Sternberg & Dalgarno (1995), who considered the chemistry within dense ($n(H_2) = 5\times10^5$ cm^{-3}) gas subject to strong ($G_o = 2\times10^5$) external FUV irradiation, but no H_2O freeze-out. In their model, H_2O is produced at $A_V = 0.6$ and $T = 800$ K by the neutral-neutral reactions, $O + H_2 \rightarrow OH + H$ and $OH + H_2 \rightarrow$

$H_2O + H$. However, the abundance of H_2O in this hot gas layer is suppressed by the high FUV field which rapidly photodissociates the water. Deeper into the cloud, i.e. at $A_V > 5$, where the FUV is attenuated and the gas temperature has dropped to $\sim 22\,K$ in their model, a series of gas-phase ion-neutral reactions produces a relatively high abundance of H_2O ($x(o–H_2O) \sim 3\times10^{-5}$) which survives photodestruction. For the sample case considered, this model would result in more than 90 percent of the water vapor emission arising between $A_V = 5$ and 20, and this fraction would be expected to increase further with increasing cloud depth. Even for a line of sight with a total depth equivalent to $A_V = 10$, approximately 80 percent of the water-vapor emission is calculated to arise at $A_V > 5$. Thus, a PDR model which considers water formed only in the gas phase, and which remains in the gas phase through the depth of the cloud, does not fit the Orion data.

To assess the case of constant water vapor abundance throughout the cloud volume, we apply the Sternberg and Dalgarno model above, except the ortho-H_2O abundance is assumed to be 5×10^{-7} (relative to H_2) and constant with depth. This value is at the high end of, but nonetheless consistent with, the range of water abundances inferred from *SWAS* observations of quiescent clouds, assuming the depths of the H_2O and H_2 regions are the same (e.g., Snell et al. 2000c). As shown in the middle panel of Fig. 17, most of the water-vapor emission originates throughout the volume of the cloud. Nonetheless, for clouds of total depth less than an A_V of about 12, more than half of the total water emission would originate in the warm surface layers (i.e., $A_V \lesssim 3$). In practice, however, the presence of a $G_o \gtrsim 100$ FUV field would destroy almost all of the water near the cloud surface, as is evident from the H_2O abundance profiles in Figs. 15 and 16, and more recently confirmed by Hollenbach et al. (2009). Thus, for the case of a constant water abundance throughout the cloud, the water emission would again be expected to increase with cloud depth, which it does not.

Third, we consider a temperature and H_2O abundance profile based on the model of Hollenbach et al. (2009), except for $n(H_2) = 5\times10^4\ cm^{-3}$ and $G_o = 10^5$. In this model, the temperature and chemical structure of a cloud are determined not only by the gas-phase chemistry, but also by the freezing of species onto grains, simple grain surface chemistry, and desorption (including

FUV photodesorption) of ices. The resulting gas-phase H_2O abundance is found to peak in a region between the cloud surface, where H_2O is photo-destroyed by FUV photons, and the deeper interior, where the FUV field is highly attenuated and gas-phase H_2O depletes rapidly onto grains as frozen water-ice (see Fig. 18). Because the sublimation temperature of water-ice is high (i.e., $\gtrsim 90\,\mathrm{K}$), it remains on the grains until sputtered off by the passage of a nondissociative shock, heated by an embedded source, photodesorbed by FUV radiation, or removed by cosmic rays. Specifically, this model predicts that the gas-phase H_2O and O_2 lies predominantly between an A_V of approximately 3 and 8 for $G_o = 1 - 10^3$, with the peak abundance occurring at a depth proportional to $\ln(G_o/n_H)$, where n_H is the gas-phase hydrogen nucleus number density. As shown in the right panel of Fig. 17, for this scenario ($G_o = 10^5$) all of the water-vapor emission is predicted to arise from within a narrow range of depths around $A_V \simeq 10$ corresponding to the peak in the gas-phase H_2O abundance. For lower values of G_o, but approximately equivalent densities, the peak gas-phase H_2O abundance shifts to lower A_V's, as shown in the center and right panels of Fig. 18. However, unlike the assumptions underlying our analysis of the Orion ridge observations, the Hollenbach et al. models shown in Fig. 18 depict steady-state abundance profiles, which include the effects of CO destruction due to He^+. Without CO depletion, these models underestimate the gas-phase H_2O and CO abundances at high A_V. However, the peak of water abundance at intermediate A_V is likely preserved, consistent with the observations.

Finally, we note that the observed C_2H and N_2H^+ transitions have similar excitation energies and critical densities (see Table 1), yet show strikingly different depth profiles (e.g., Figs. 11 and 12). Thus, the variations in their depth-dependent integrated intensity profiles are not the result of excitation conditions.

Limits to the assumption of a simple homogeneous slab geometry, illuminated from one side, are also seen in the data. Specifically the intensity ratios for species such as CI, CN, HCN, and C_2H exhibit values at high A_V's (e.g., $\gtrsim 15$ mag.) that exceed those expected on the basis of their low deep-cloud abundances as shown in Figs. 15 and 16. This is most likely the result of the Orion ridge being somewhat clumpy (cf. Stacey et al. 1993, and references therein), permitting partial penetration of FUV photons deep into the cloud interior. In addition, B stars embedded

within the molecular cloud may provide additional FUV flux. Thus, emission characteristic of predominately surface tracers can still be generated, albeit at a lower intensity, well within the cloud interior. In addition, if the effects of H_2O freeze-out are added to the models shown in Figs. 15 and 16, the deep-cloud abundance of CI, CN, HCN, and C_2H may be altered. This effect notwithstanding, the derived emission profiles for these species follow the trends predicted from PDR models, at least up to the depth where H_2O freezes out.

The conclusion that ground-state water-vapor emission is observed to arise primarily near molecular cloud surfaces is in accord with models, like Hollenbach et al. (2009), in which the gas-phase water abundance peaks where rates of photodestruction, photodesorption, and freeze-out balance. In this model, the distance from the cloud surface to the peak water-vapor abundance scales as $\ln(G_o/n_H)$ and the range of depths over which the water vapor is relatively abundant is self regulating and remains approximately constant. Consequently, the water-vapor column density remains approximately constant over a broad range of FUV fluxes and densities, thus explaining the relatively narrow distribution of observed H_2O $1_{10}-1_{01}$ peak antenna temperatures.

This picture is also consistent with the low observed upper limits to the O_2 abundance (Goldsmith et al. 2000). Since the ion-neutral reactions leading to the formation of O_2 depend upon the abundance of gas-phase O (via the reaction $O + OH \rightarrow O_2 + H$), reducing the atomic oxygen abundance by locking it in water ice suppresses O_2 production where water ice becomes abundant – i.e., beyond an A_V of ~ 2 to 10. Thus, like water vapor, gas-phase O_2 is restricted to a relatively narrow zone between where it's photodestroyed near the cloud surface and where its formation is suppressed by a diminishing supply of atomic oxygen . Detailed calculations (e.g., Hollenbach et al. 2009) indicate that the resulting O_2 column densities are typically between 10^{15} and 10^{16} cm^{-2}, consistent with current observed limits.

Finally, evidence supporting an increasing column density of water-ice with depth is provided by observations of the water-ice band at 3 μm toward Taurus (Whittet et al. 2001) and Rho Ophiuchus (Tanaka et al. 1990), and the water-ice band at 6 μm toward Cepheus A East (Sonnentrucker et al. 2008). The onset for water-ice formation toward Taurus, Rho Ophiuchus,

and Cepheus A East is determined to occur at A_V's of 3.2, ~ 10, and 2.3 visual magnitudes, respectively, with the variation due primarily to the different FUV radiation environments for each cloud. These observations also confirm the presence of significant amounts of water-ice (x(H$_2$O–ice) $> 5 \times 10^{-5}$) in the deep interior of dense clouds (e.g., Nummelin et al. 2001; Boogert et al. 2004; Sonnentrucker et al. 2008). The detection of CO$_2$ ice with an abundance of $\sim 2 \times 10^{-5}$ (Boogert et al. 2004; Sonnentrucker et al. 2008) further attests to the importance of ices as a repository of oxygen that would otherwise be available to form gas-phase H$_2$O and O$_2$.

In summary, the results of the observational study presented here show that most of the water vapor detected toward the Orion Molecular Cloud ridge originates near the cloud surface, between an A_V of about 2 and 10. This finding is in general agreement with PDR models that consider the effects of photodissociation, grain-surface chemistry, photodesorption, and freeze-out in addition to gas-phase chemistry. Future observations with the *Herschel Space Observatory* will allow more detailed follow-up studies of the water-vapor distribution in molecular clouds in several ways. First, *Herschel*'s smaller beam size at 557 GHz – 40″ versus $\sim 230''$ for *SWAS* – will permit many more spatial samples than obtained here, improving the statistics for the type of analysis applied here. Second, access to additional ortho- and para-H$_2$O transitions will enable a more direct determination of the physical conditions in the water-vapor emitting region. Combined, these capabilities will allow increasingly stringent tests of our models of water in molecular clouds.

REFERENCES

Bally, J., Langer, W.D., Stark, A.A., & Wilson, R.W. 1987, *Ap. J.*, 312, L45

Benedettini, M., Viti, S., Giannini, T., Nisini, B., Goldsmith, P.F., & Saraceno, P. 2002, *A&A*, 395, 657

Bergin, E.A., Alves, J., Huard, T., & Lada, C.J. 2002, *Ap. J.*, 570, L101

Bergin, E.A., Goldsmith, P.F., Snell, R.L., & Ungerechts, H. 1994, *Ap. J.*, 431, 674

Bergin, E. A., et al. 2000, *Ap. J. Letters*, 539, L129

Bergin, E.A., Maret, S., van der Tak, F.F.S., Alves, J., Carmody, S.M., & Lada, C.J. 2006, *Ap. J.*, 645, 369

Bergin, E.A., Snell, R.L., & Goldsmith, P.F. 1996, *Ap. J.*, 460, 343

Blake, G. A., Sutton, E. C., Masson, C.R., & Phillips, T. G. 1987, *Ap. J.*, 315, 621

Boger, G.I., & Sternberg, A. 2005, *Ap. J.*, 632, 302

Boogert, A.C.A, et al. 2004, *Ap. J. Suppl.*, 154, 359

Caselli P., Walmsley C. M., Tafalla M., Dore L., Myers P. C. 1999, *Ap. J.*, 523, L165

Dubernet, M.-L., Daniel, F., Grosjean, A., Faure, A., Valiron, P., Wernli, M., Wiesenfeld, L., Rist, C., Noga, J., & Tennyson, J. 2006, *A&A*, 460, 323

Dutrey, A., Langer, W.D., Bally, J., Duvert, G., Castets, A., & Wilson, R.W. 1991, *A&A*, 247, L9

Elitzur, M., & de Jong, T. 1978, *A&A*, 67, 323

Elitzur, M., & Watson, W.D. 1978, *A&A*, 70, 443

Erickson, N. R., Grosslein, R. M., Erickson, R. B., & Weinweb, S. 1999, IEEE Trans. Microwave Theory and Tech., 47, 2212

Faure, A., Crimier, N., Ceccarelli, C., Valiron, P., Wiesenfeld, L., & Dubernet, M. L. 2007, *A&A*, 472, 1029

Franklin, J., Snell, R.L., Kaufman, M.J., Melnick, G.J., Neufeld, D.A., Hollenbach, D.J., Bergin, E.A. 2008, *Ap. J.*, 674, 1015

Goldsmith, P. F., et al. 2000, *Ap. J. Letters*, 539, L123

Harjunpää, P., Lehtinen, K., Haikala, L. K. 2004, *A&A*, 421, 1087

Harwit, M., Neufeld, D.A., Melnick, G.J., & Kaufman, M.J. 1998, *Ap. J.*, 497, L105

Hawkins, I., & Jura, M. 1987, *Ap. J.*, 317, 926

Hollenbach, D.J., Kaufman, M. J., Bergin, E.A., & Melnick, G.J. 2009, *Ap. J.*, 690, 1497

Hummer, D.G., & Rybicki, G. 1982, *Ap. J.*, 254, 767

Jansen, D.J., Van Dishoeck, E.F., Black, J.H., Spaans, M., & Sosin, C. 1995, *A&A*, 302, 223

Jansen, D.J., Spaans, M., Hogerheijde, M.R., Van Dishoeck, E.F. 1995, *A&A*, 303, 541

Johnstone, D., & Bally, J. 1999, *Ap. J.*, 510, L49

Kainulainen, J., Lehtinen, K. & Harju, J. 2006, *A&A*, 447, 597

Keene, J., Blake, G.A., Phillips, T.G., Huggins, P.J., & Beichman, C.A. 1985, *Ap. J.*, 299, 967

Kramer C., Alves J., Lada C. J., Lada E. A., Sievers A., Ungerechts H., Walmsley C. M. 1999, *A&A*, 342, 257

Lada, C.J., Lada, E.A., Clemens, D.P., & Bally, J. 1994, *Ap. J.*, 429, 694

Langer,W. D., & Penzias, A. A. 1990, *Ap. J.*, 357, 477

Linke, R.A., Goldsmith, P.F., Wannier, P.G., Wilson, R.W., & Penzias, A.A. 1977, *Ap. J.*, 214, 50

Melnick, G.J., Ashby, M.L.N., Plume, R., Bergin, E.A., Neufeld, D.A., Chin, G., Erickson, N.R., Goldsmith, P.F., Harwit, M., Howe, J.E., Kleiner, S.C., Koch, D.G., Patten, B.M., Schieder, R., Snell, R.L., Stauffer, J.R., Tolls, V., Wang, Z., Winnewisser, G., & Zhang, Y.F. 2000, *Ap. J.*, 539, L87

Melnick, G.J., et al. 2000, *Ap. J.*, 539, L77

Melnick, G.J. 2004, *Advances in Space Research*, 34, 511

Melnick, G.J., Tolls, V., Neufeld, D.A., Yuan, Y., Sonnentrucker, P., Watson, D.M., Bergin, E.A., & Kaufman, M.J. 2008, *Ap. J.*, 683, 876

Mookerjea, B., Ghosh, S.K., Rengarajan, T.N., Tandon, S.N., & Verma, R.P. 2000, *A. J.*, 120, 1954

Morata, O., & Herbst, E. 2008, *M.N.R.A.S.*, 390, 1549

Neufeld, D.A., Snell, R.L., Ashby, M.L.N., Bergin, E.A., Chin, G., Erickson, N.R., Goldsmith, P.F., Harwit, M., Howe, J.E., Kleiner, S.C., Koch, D.G., Patten, B.M., Plume, R., Schieder, R., Stauffer, J.R., Tolls, V., Wang, Z., Winnewisser, G., Zhang, Y.F., & Melnick, G.J. 2000, *Ap. J.*, 539, L107

Neufeld, D. A., et al. 2000a, *Ap. J. Letters*, 539, L111

Neufeld, D. A., Bergin, E. A., Melnick, G. J., & Goldsmith, P. F. 2003, *Ap. J.*, 590, 882

Neufeld, D.A., et al. 2000, *Ap. J. Letters*, 539, L111

Neufeld, D.A., Hollenbach, D.J., Kaufman, M.J., Snell, R.L., Melnick, G.J., Bergin, E.A., & Sonnentrucker, P. 2007, *Ap. J.*, 664, 890

Neufeld, D.A., Kaufman, M.J., Goldsmith, P.F., Hollenbach, D.J. & Plume, R. 2002, *Ap. J.*, 580, 278

Neufeld, D.A., Lepp, S., & Melnick, G.J. 1995, *Ap. J. Suppl.*, 100, 132

Neufeld, D.A., & Melnick, G.J. 1987, *Ap. J.*, 322, 266

Neufeld, D.A., & Melnick, G.J. 1991, *Ap. J.*, 368, 215

Nisini, B., Benedettini, M., Giannini, T., Codella, C., Lorenzetti, D., Di Giorgio, A.M., & Richer, J.S. 2000, *A&A*, 360, 297

Nummelin, A., Whittet, D.C.B., Gibb, E.L., Gerakines, P.A., & Chiar, J.E. 2001, *Ap. J.*, 558, 185

Pineda, J.E., Caselli, P., & Goodman, A.A. 2008, *Ap. J.*, 679, 481

Pineda, J.L., Goldsmith, P.F., Chapman, N., Snell, R.L., Li, D., Cambrésy, L., & Brunt, C. 2010, arXiv:1007.5060v1

Plume R., et al. 2000, *Ap. J. Letters*, 539, L133

Poelman, D.R., Spaans, M., & Tielens, A.G.G.M. 2007, *A&A*, 464, 1023

Rodríguez-Franco, A., Martín-Pintado, V., & Fuente, A. 1998, *A&A*, 329, 1097

Savage, C., Apponi, A.J., Ziurys, L.M., & Wyckoff, S. 2002, *Ap. J.*, 578, 211

Schöier, F.L., Van der Tak, F.F.S., van Dishoeck, E.F. & Blaqck, J. H., 2005, *A&A*, 432, 369

Snell, R. L., et al. 2000, *Ap. J. Letters*, 539, L93

Snell, R. L., et al. 2000, *Ap. J. Letters*, 539, L97

Snell, R. L., et al. 2000, *Ap. J. Letters*, 539, L101

Sonnentrucker, P., Neufeld, D.A., Gerakines, P.A., Bergin, E.A., Melnick, G.J., Forrest, W.J., Pipher, J.L., Whittet, D.C.B. 2008, *Ap. J.*, 672, 361

Stacey, G.J., Jaffe, D.T., Geis, N., Grenzel, R., Harris, A.I., Poglitsch, A., Stutzki, J., & Townes, C. H. 1993, *Ap. J.*, 404, 219

Sternberg, A. & Dalgarno, A. 1995, *Ap. J. Suppl.*, 99, 565

Tafalla, M., Myers, P.C., Caselli, P., & Walmsley, C.M. 2004, *A&A*, 416, 191

Tanaka, M., Sato, S., Nagata, T., & Yamamoto, T. 1990, *Ap. J.*, 352, 724

Tatematsu, K., et al. 1993, *Ap. J.*, 404, 643

Tielens, A. G. G. M., Tokunaga, A. T., Geballe, T. R., & Baas, F. 1991, *Ap. J.*, 381, 181

Tolls, V., et al., 2004, *Ap. J. Suppl.*, 152, 137

Ungerechts, H., Bergin, E.A., Goldsmith, P.F., Irvine, W.M., Schloerb, F.P., & Snell, R.L. 1997, *Ap. J.*, 482, 245

Van der Tak, F.F.S., Black, J.H., Schöier, F.L., Jansen, D.J. & van Dishoeck, E.F., 2007, *A&A*, 468, 627

Whittet, D.C.B. et al. 1998, *Ap. J.*, 498, L159

Whittet, D.C.B., Gerakines, P.A., Hough, J.H., & Shenoy, S.S. 2001, *Ap. J.*, 547, 872

Willacy K., Langer W. D., & Velusamy T. 1998, *Ap. J.*, 507, L171

Zinchenko, I., Caselli, P., & Pirogov, L. 2009, *M.N.R.A.S.*, 395, 2234
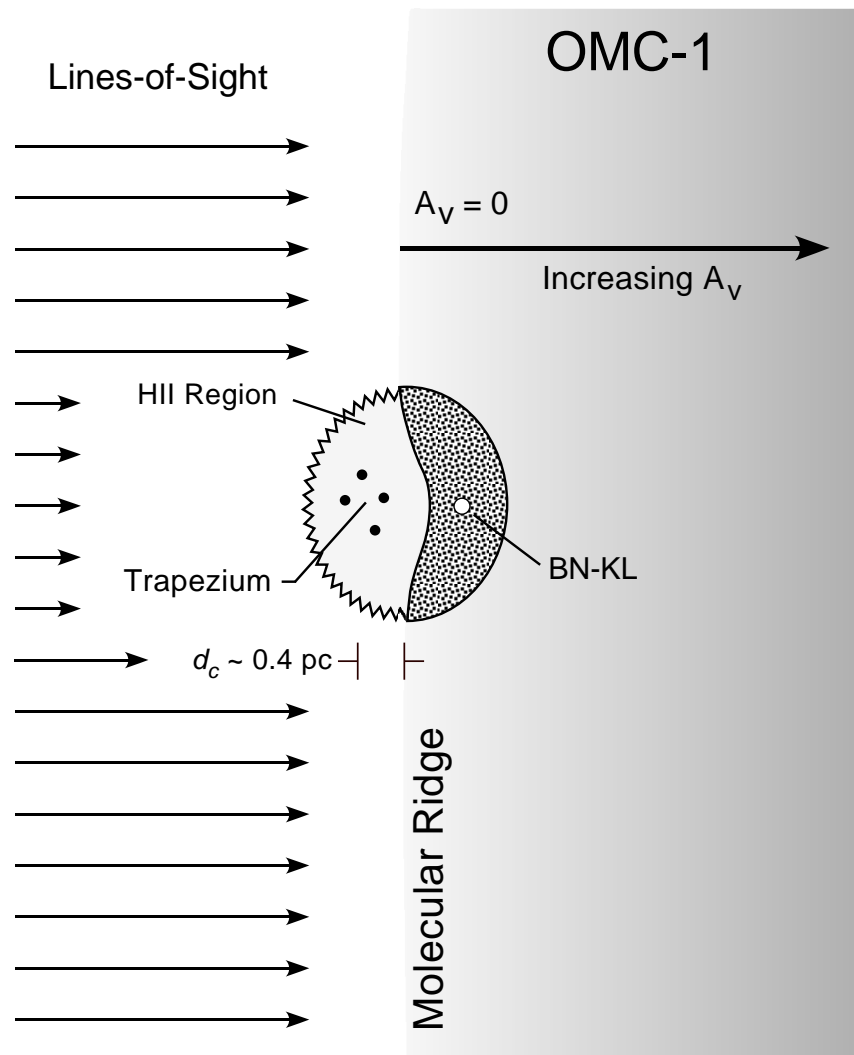
Fig. 1. Schematic representation of the lines-of-sight from earth in relation to the structure of the Orion Molecular Cloud ridge. The face-on geometry of the molecular ridge permits a relatively straightforward comparison of the distribution of tracers as a function of A_V. The distance between the Trapezium cluster and the ridge, d_c, is noted.
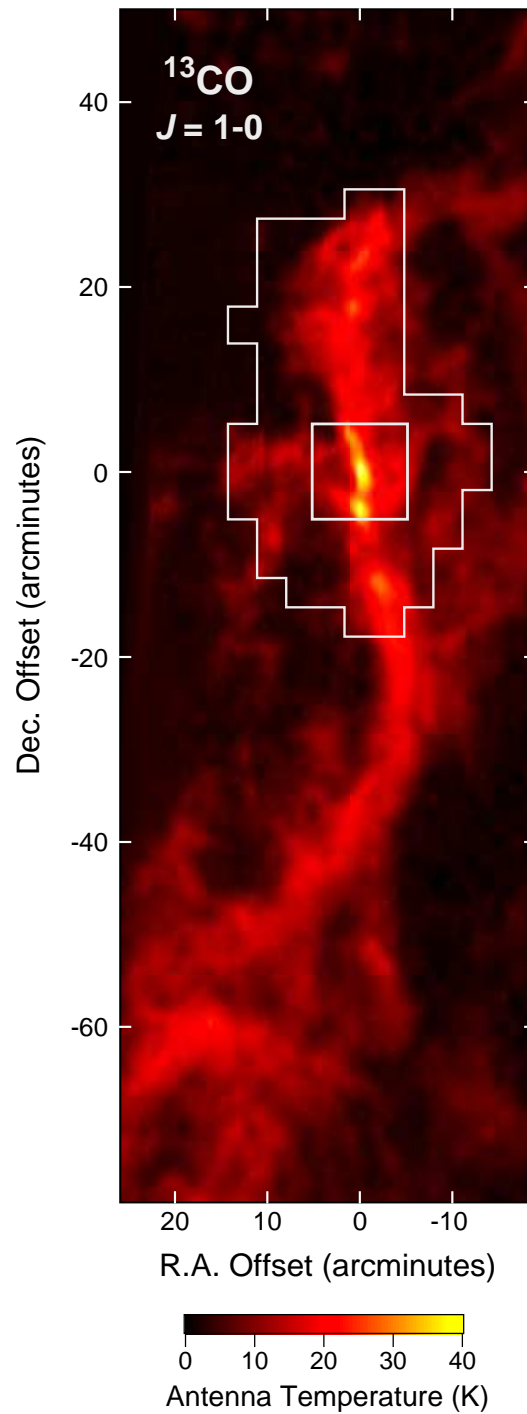
Fig. 2. Integrated intensity map of the Orion Molecular Ridge made in the ^{13}CO $J = 1$-0 110.2 GHz transition using the Five College Radio Astronomy Observatory (see Table 1). The beamsize was $47''$. The larger grey-outlined region encompasses the region mapped in the $H_2^{16}O$ 1_{10}-1_{01} 556.9 GHz transition by *SWAS*. The inner region, denoted by the grey square, includes gas also subject to strong outflow shocks and is not included in the analysis. All offsets are relative to $\alpha = 05^h35^m14\overset{s}{.}5$, $\delta = -05°22'37''$ (J2000).
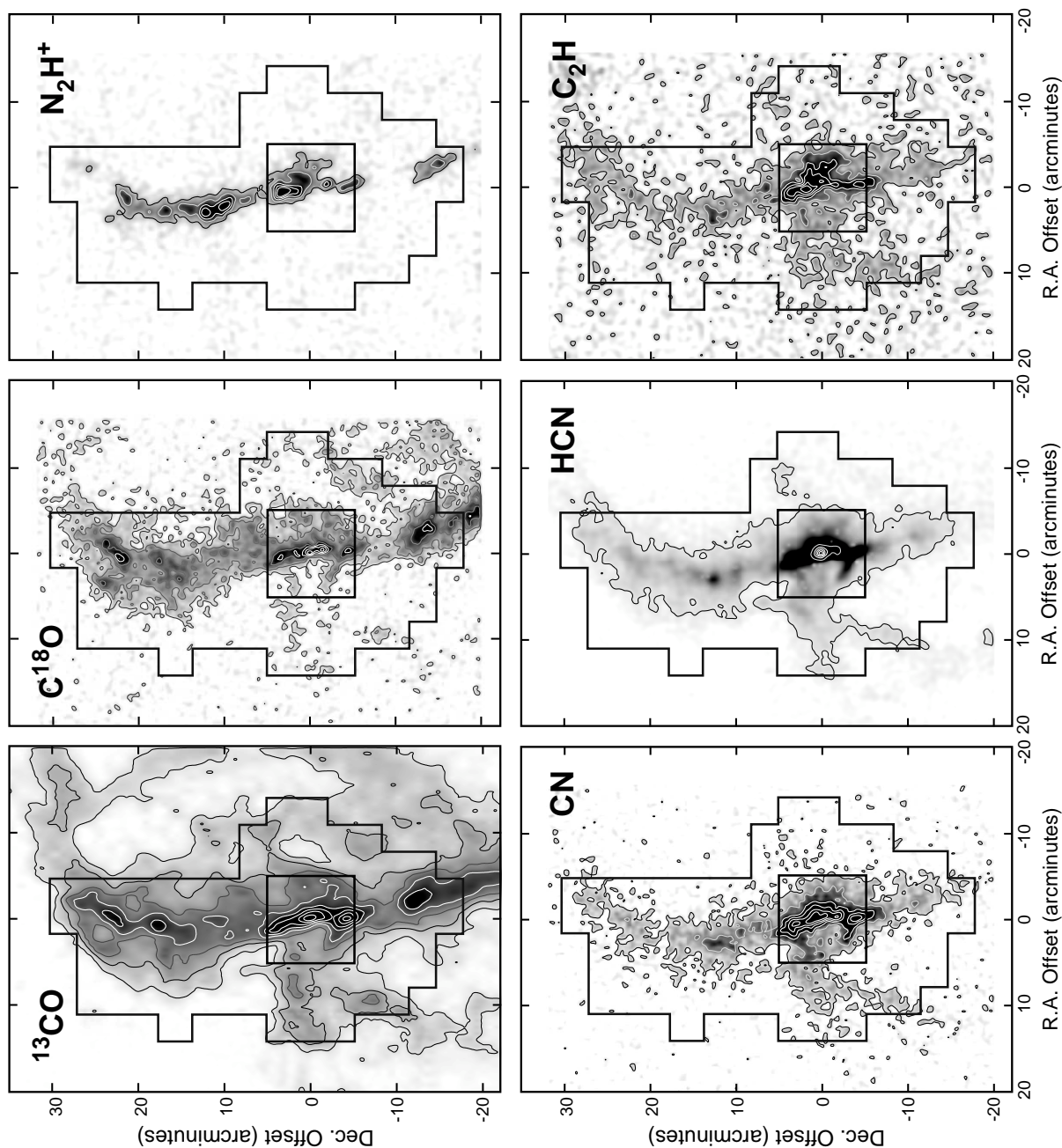
Fig. 3. Maps of the Orion Molecular Ridge obtained with $46'' - 60''$ spatial resolution using the Five College Radio Astronomy Observatory (see Table 1). The peak integrated intensities ($\int T_A^* \, dv$), in K km s^{-1}, are: 47.39 (^{13}CO), 6.896 (C^{18}O), 14.16 (N$_2$H$^+$), 29.85 (CN), 325.3 (HCN), 6.556 (C$_2$H). Contours superposed on the ^{13}CO and C^{18}O maps are in units of 0.10 of the peak value, with the peak contour shown being 0.9. Contours superposed on the N$_2$H$^+$, CN, HCN, and C$_2$H maps are in units of 0.15 of the peak value. The larger outlined region encompasses the region mapped in the H$_2^{16}$O 1$_{10}$-1$_{01}$ 556.9 GHz transition by *SWAS*. The inner region, denoted by the square, includes gas also subject to strong outflow shocks and is not included in the analysis. All offsets are relative to $\alpha = 05^h35^m14.5^s$, $\delta = -05°22'37''$ (J2000).
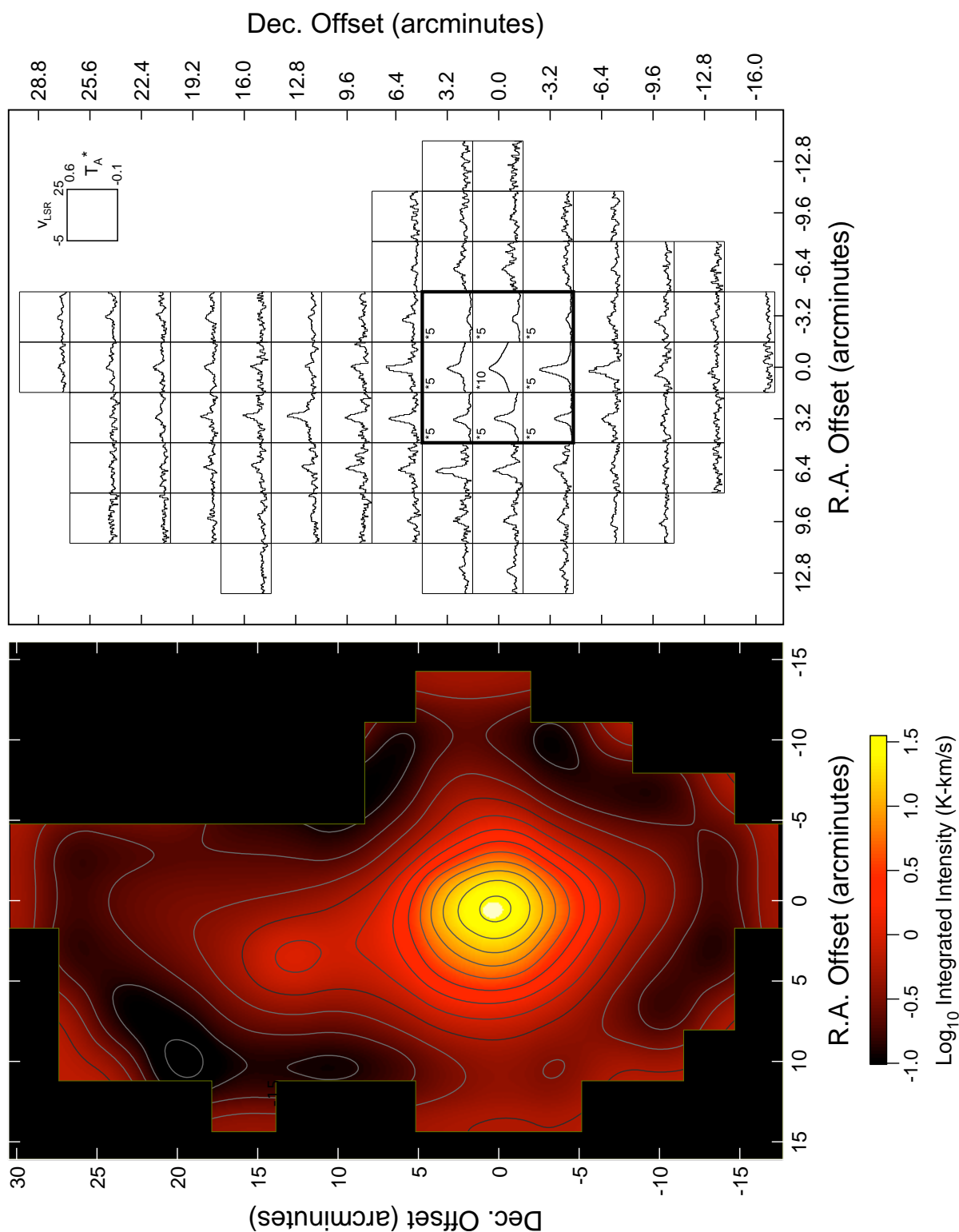
Fig. 4. Integrated intensity map of the Orion Molecular Ridge in $H_2^{16}O$ 1_{10}-1_{01} 556.9 GHz transition using *SWAS* (see Table 1). The inner region, denoted by the bolded square encompassing the spectra centered on position (0, 0) in the right panel, includes gas also subject to strong outflow shocks and is not included in the analysis. The starred numbers within this square indicate the values by which the antenna temperatures have been divided so that the scaled spectra fit within this plot. All offsets are relative to $\alpha = 05^h35^m14\fs5$, $\delta = -05^\circ22'37''$ (J2000).
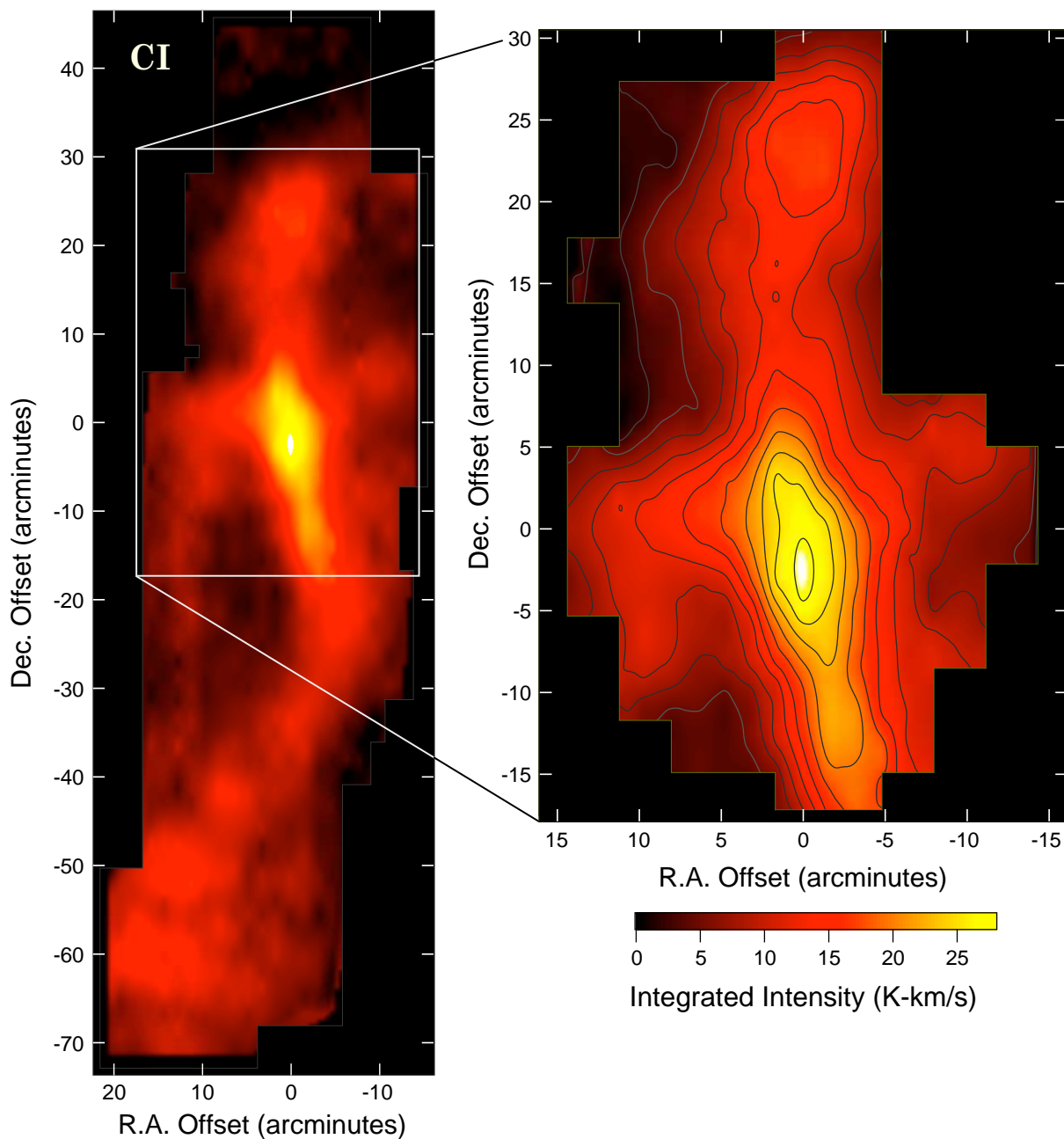
Fig. 5. *Left: SWAS* integrated intensity map of the Orion Molecular Ridge in the CI $^3P_1-^3P_0$ 492.2 GHz transition (see Table 1). *Right:* Subset of the extended *SWAS* CI map obtained with the longer integration times used to measure the $H_2^{16}O$ $1_{10}-1_{01}$ 556.9 GHz emission. The peak CI integrated intensity is 28.3 K km s^{-1} and the contours are in increments of 2.5 K km s^{-1} from zero integrated intensity. All offsets are relative to $\alpha = 05^h35^m14^s.5$, $\delta = -05°22'37''$ (J2000).
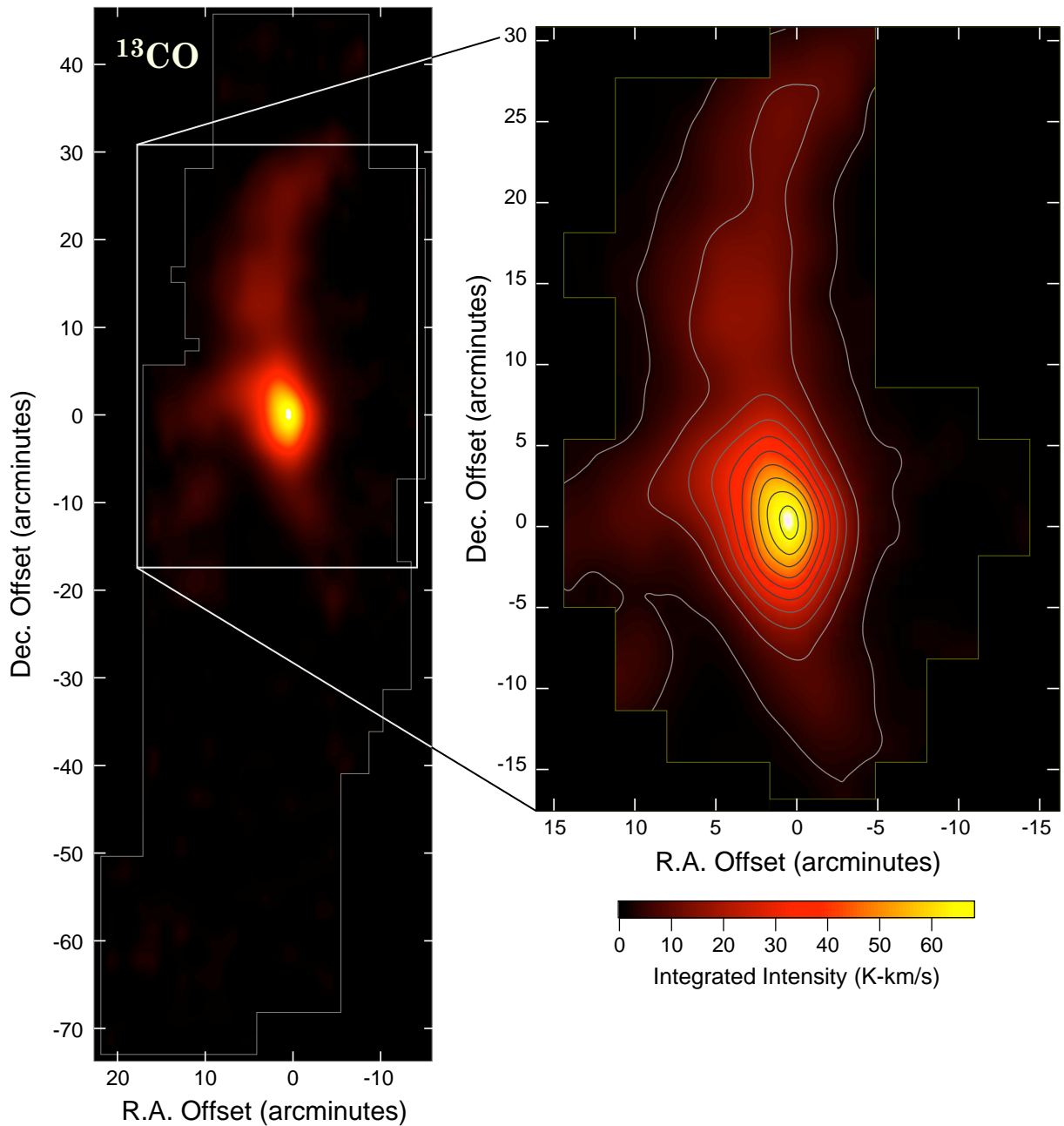
Fig. 6. *Left: SWAS* integrated intensity map of the Orion Molecular Ridge in the ^{13}CO $J = 5 - 4$ 550.9 GHz transition (see Table 1). *Right:* Subset of the extended *SWAS* ^{13}CO $J = 5 - 4$ map obtained with the longer integration times used to measure the $H_2^{16}O$ 1_{10}-1_{01} 556.9 GHz emission. The peak ^{13}CO $J = 5 - 4$ integrated intensity is 69.1 K km s^{-1} and the contours are in increments of 7 K km s^{-1} from an integrated intensity of 3 K km s^{-1}. All offsets are relative to $\alpha = 05^h35^m14\overset{s}{.}5$, $\delta = -05°22'37''$ (J2000).
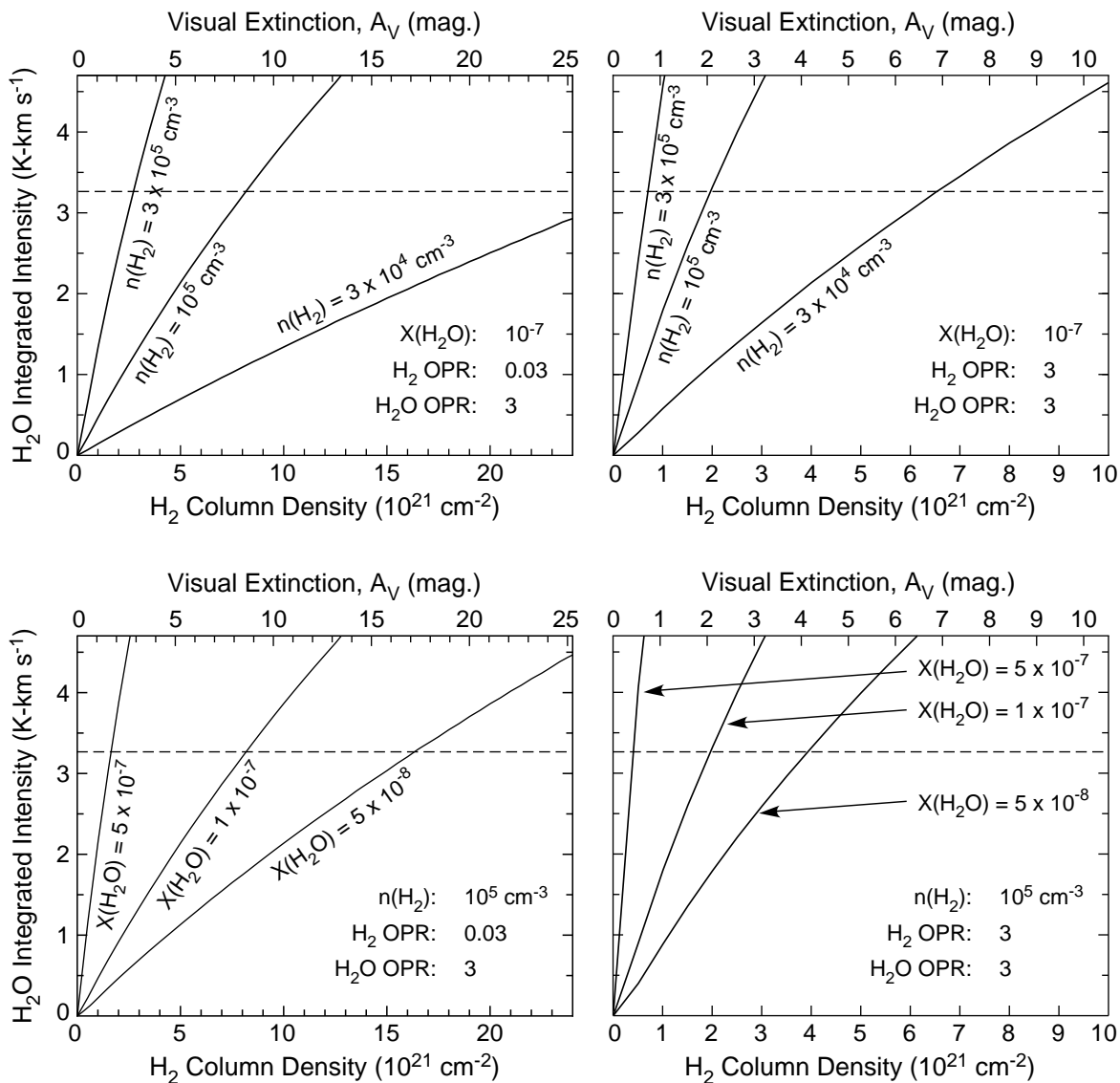
Fig. 7. Plots of computed H_2O $1_{10}-1_{01}$ integrated antenna temperature for a Gaussian line, $1.064 \times \int T_A dv$, versus H_2 column density. The calculations assume a slab geometry, a gas temperature of 30 K, and a line width of 3.5 km s^{-1}. The horizontal dashed line in each plot denotes the maximum integrated antenna temperature measured among the 77 spatial positions sampled, 3.26 K km s^{-1}. Thus, the H_2O integrated intensities from all observed positions can be reproduced by conditions below the dashed line. *Upper left*: Curves of $\int T_A dv$ vs. $N(H_2)$ for $X(H_2O)=10^{-7}$, an H_2 OPR=0.03, the LTE value at $T=30$ K, an H_2O OPR=3, and H_2 densities of 3×10^4, 10^5, and 3×10^5 cm^{-3}. *Upper right*: Same as the *upper left* plot, except the H_2 OPR is assumed to be 3. *Lower left*: Curves of $\int T_A dv$ vs. $N(H_2)$ for $n(H_2)=10^5$, an H_2 OPR=0.03, an H_2O OPR=3, and assumed total (ortho+para) H_2O abundances of 5×10^{-8}, 10^{-7}, and 5×10^{-7}. *Lower right*: Same as the *lower left* plot, except the H_2 OPR is assumed to be 3. The depth into the cloud, measured in magnitudes of visual extinction, assumes $N(H_2) = 9.5 \times 10^{20} A_V$ cm^{-2}.
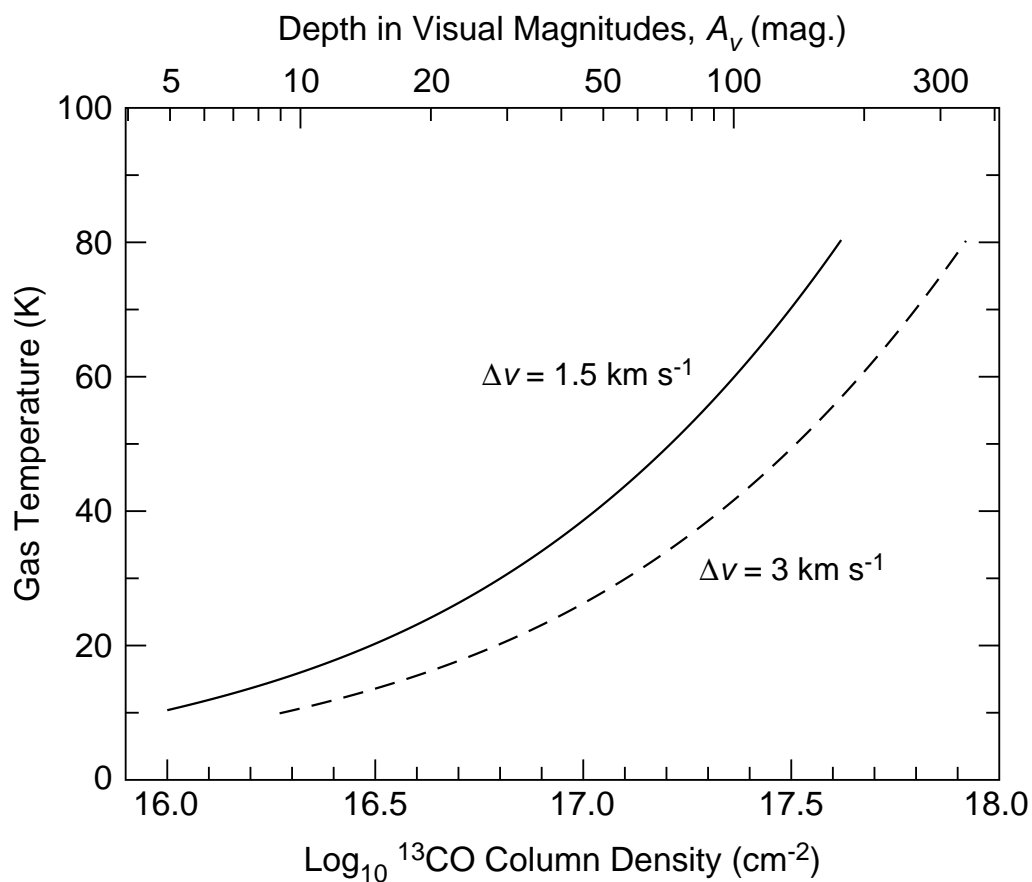
Fig. 8. Plot of the column density required to reach an optical depth of 1 in the ^{13}CO $J = 1-0$ transition as a function of the gas temperature for line widths of 1.5 and 3 km s^{-1} (see text). The relation between the ^{13}CO column density and the depth into the cloud, measured in magnitudes of visual extinction, is that provided in Pineda et al. (2008).
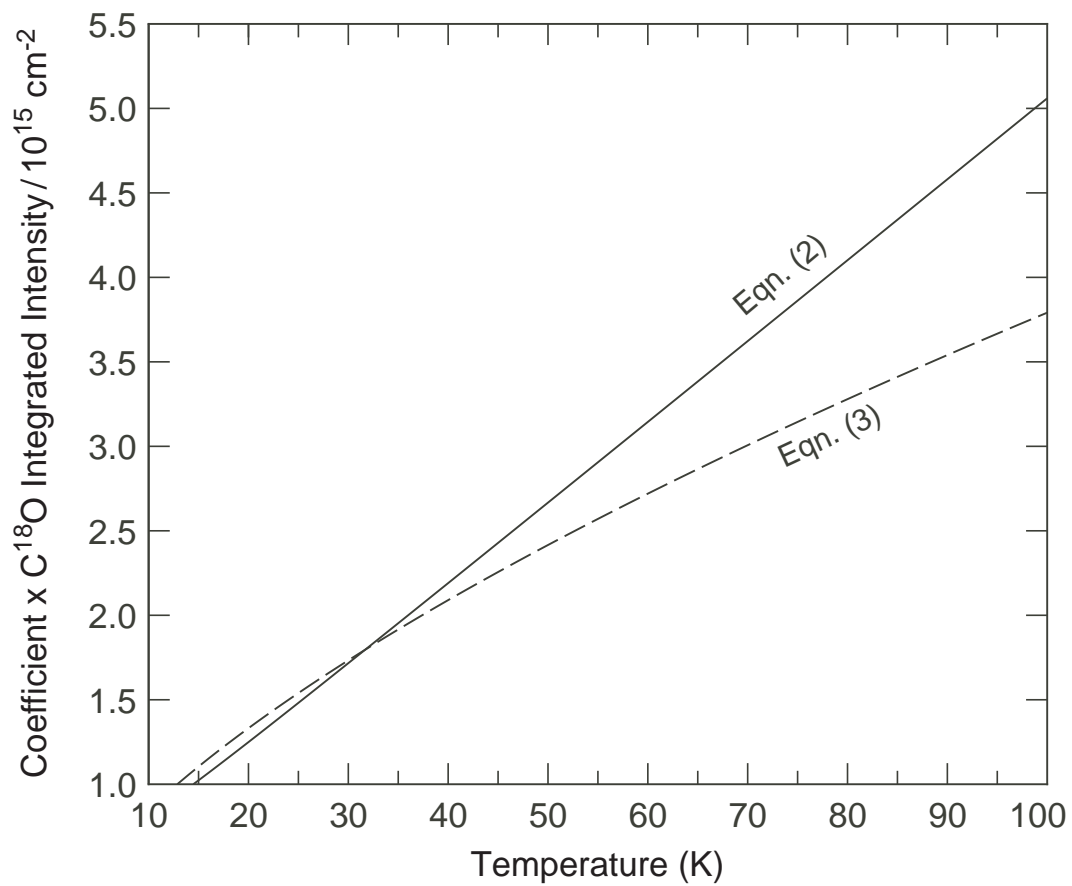
Fig. 9. Comparison of the leading terms in Eqns. (2) and (3), which provide two different approaches to connecting the $C^{18}O$ column density, $N(C^{18}O)$, to the integrated intensity of the $C^{18}O$ $J = 1-0$ line.
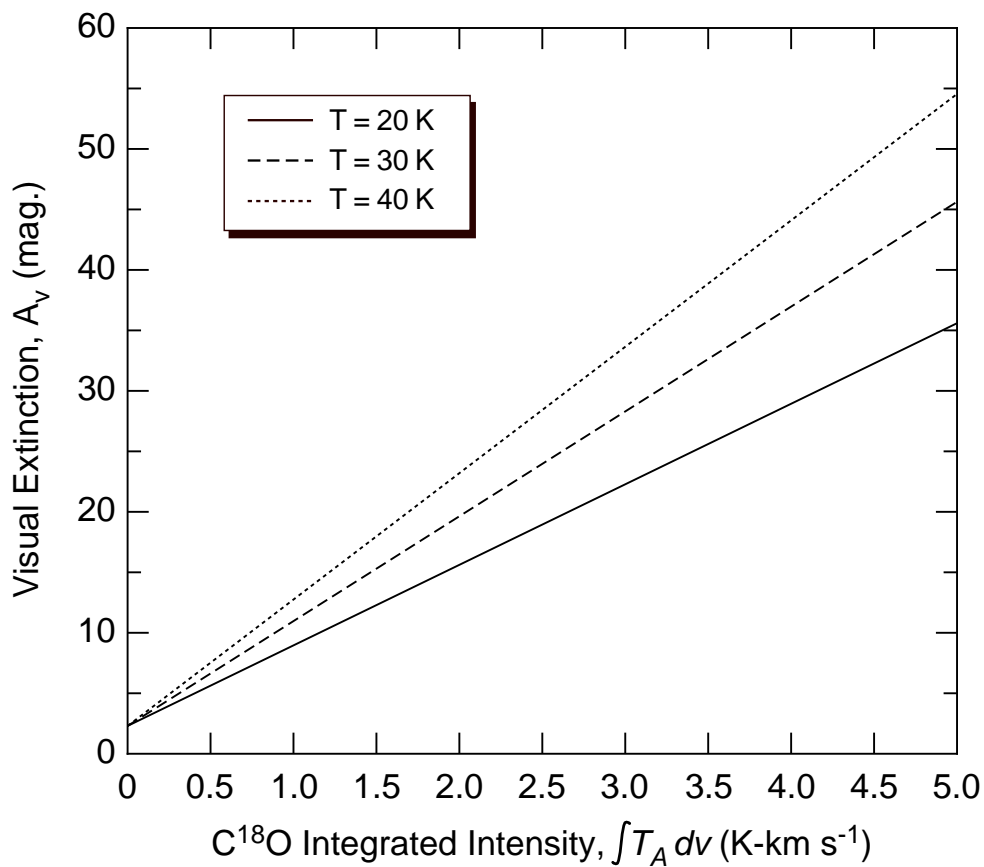
Fig. 10. Plot of temperature-dependent relation between the visual extinction, A_V, and the $C^{18}O$ integrated intensity, $\int T_A dv$ (K km s^{-1}), given in Eqn. (4), corrected for the main-beam efficiency, 0.5, at the $C^{18}O$ frequency. A temperature of 30 K is assumed in our analysis. The measured $C^{18}O$ integrated intensities toward the positions considered in this study are all less than 4 K km s^{-1}.
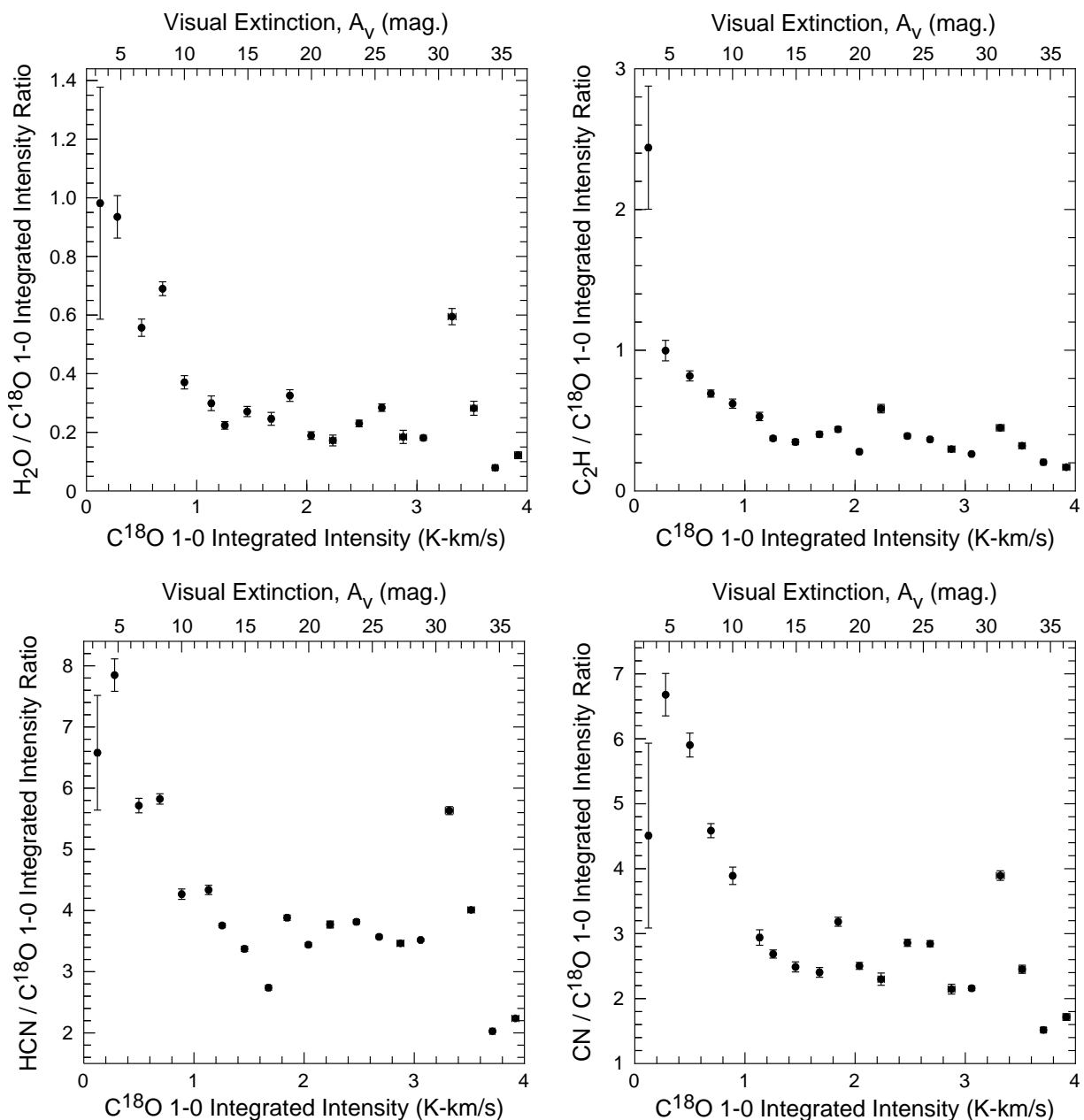
Fig. 11. Plots of the ratio of the H_2O, C_2H, HCN, and CN integrated intensities to the $C^{18}O$ $J = 1-0$ integrated intensity versus the $C^{18}O$ $J = 1-0$ integrated intensity. Using Eqn. (4) and assuming a gas temperature of 30 K, the ratios are also presented as a function of visual magnitude, A_V. The 77 spatial positions observed have been binned according to their $C^{18}O$ integrated intensities and co-averaged in 20 equal x-axis bins of 0.2 K km s^{-1} to reduce the dispersion in each plot. The x-y error bars for each point represent the error-weighted mean and 1σ uncertainty in the mean for the co-averaged points in each bin. The high point at a $C^{18}O$ integrated intensity of 3.3 K km s^{-1} represents one spatial sample corresponding to position $\Delta\alpha, \Delta\delta = 6.4, 0$. The proximity of this one sight line to BN/KL is likely responsible for the elevated ratio values seen in these plots.
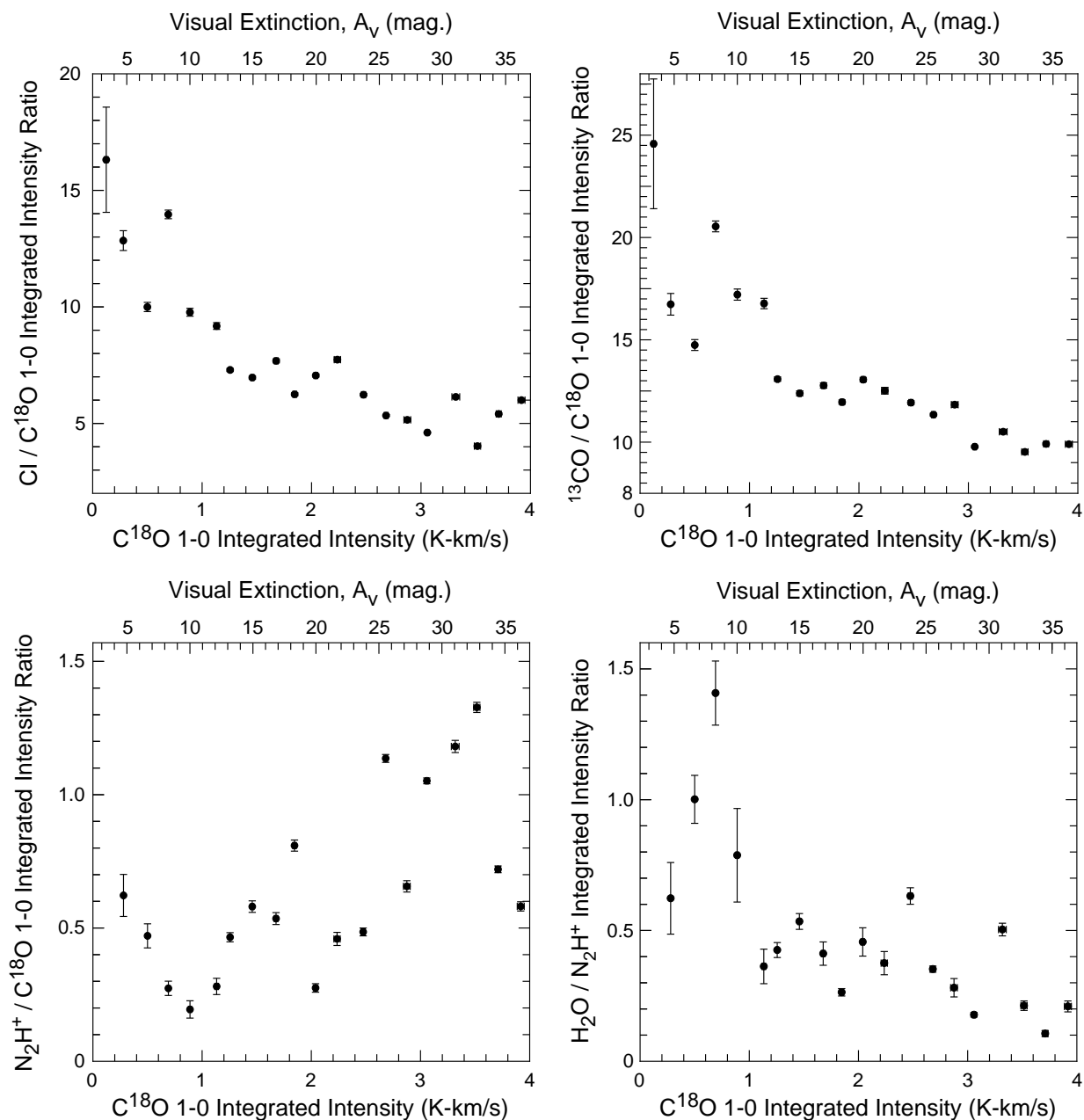
Fig. 12. Same as Fig. 11, except for the ratio of the CI, ^{13}CO, and N_2H^+ integrated intensities to the $C^{18}O$ J =1-0 integrated intensity and the H_2O to N_2H^+ integrated intensities to the $C^{18}O$ J =1-0 integrated intensity. Note that one point at the lowest $C^{18}O$ integrated intensity is excluded from the bottom two panels due to the absence of detectable N_2H^+ emission from these positions.
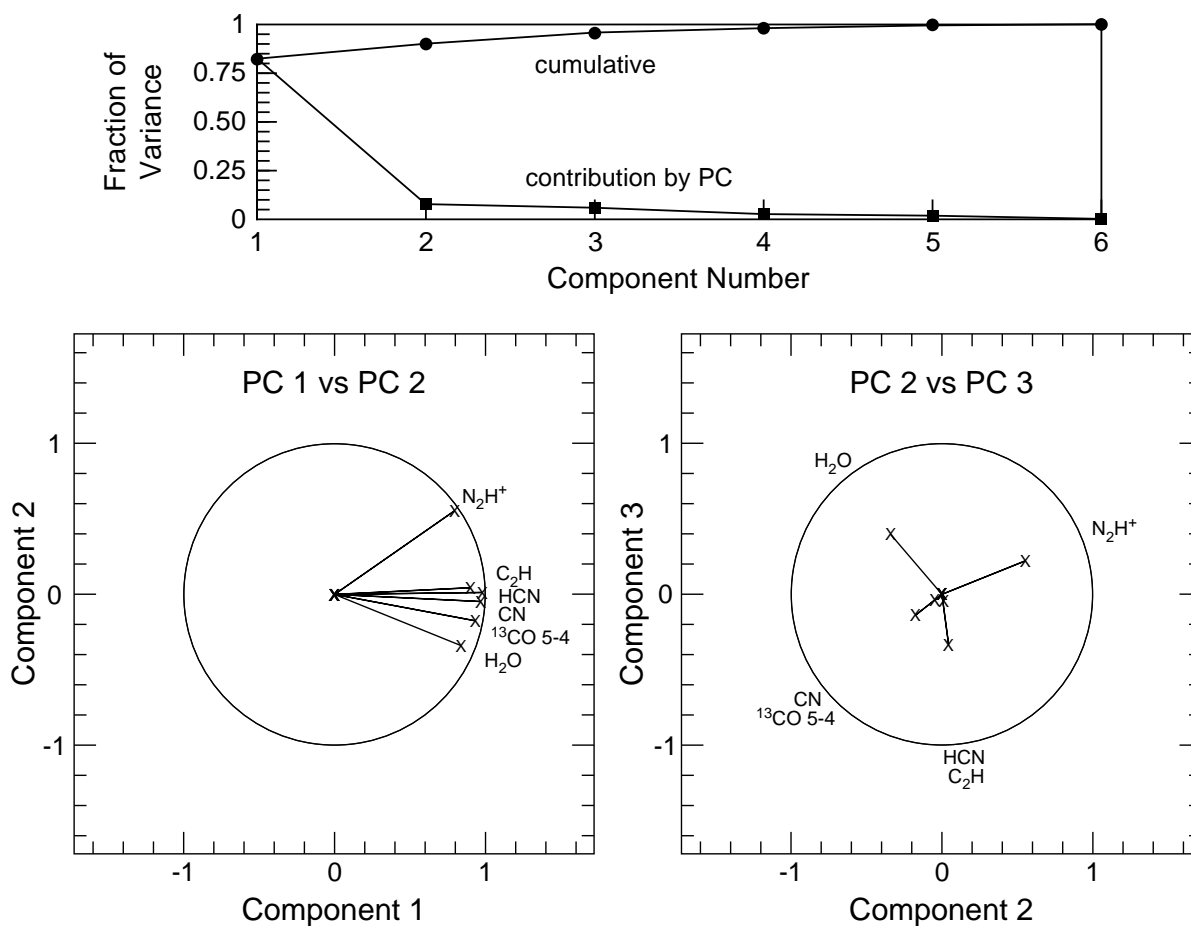
Fig. 13. Results of PCA analysis for high (i.e., $> 10^4 \text{cm}^{-3}$) critical density species. *Top*: Fraction of the total variance accounted for by each principal component, along with the cumulative fraction for the first n principal components as a function of n. *Bottom left*: Coefficients for the first and second principal components needed to approximate the maps of each transition. *Bottom right*: Coefficients for the second and third principal components.
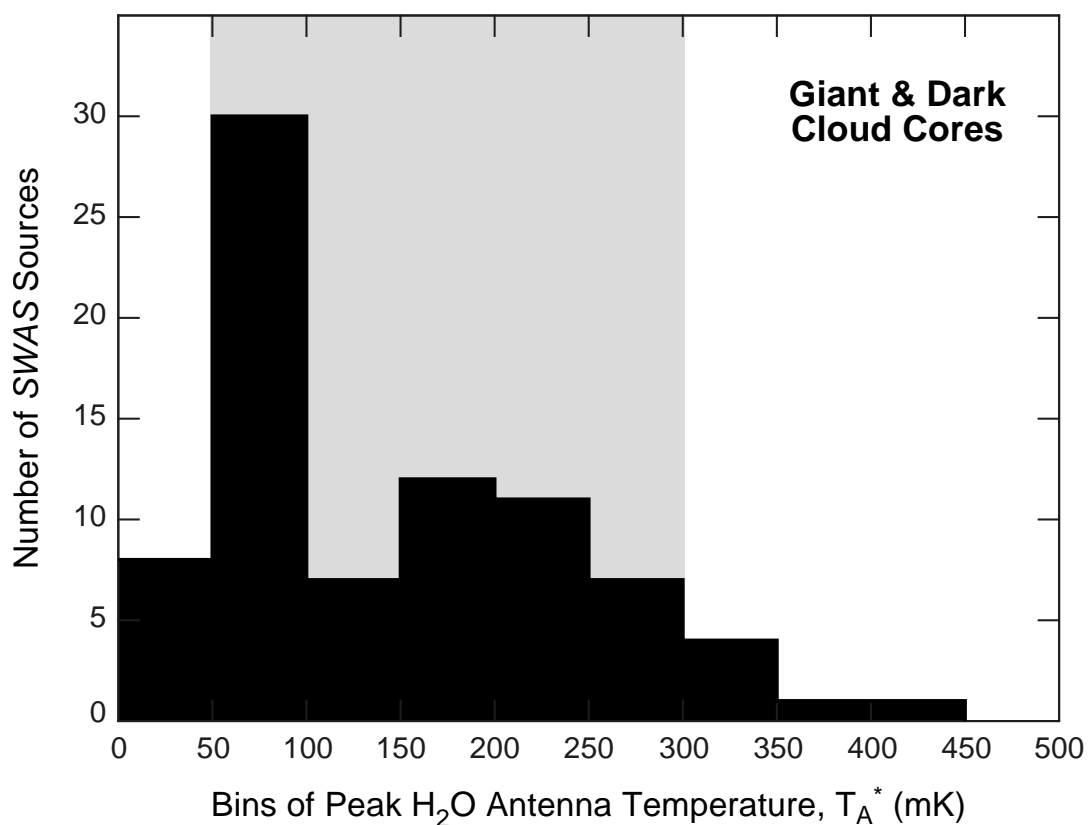
Fig. 14. Histogram of peak $H_2^{16}O$ $1_{10}-1_{01}$ 556.9 GHz antenna temperatures, T_A^*, measured toward 83 dark and giant cloud cores by *SWAS*. Almost 70 percent of the sources were observed to have peak T_A^*'s within a factor of two of 100 mK, while more than 80 percent of the sources exhibit peak T_A^*'s between 50 and 300 mK (grey area). This distribution is much narrower than would be expected based on the spread of column densities and volume densities of the sources in the sample (see text).
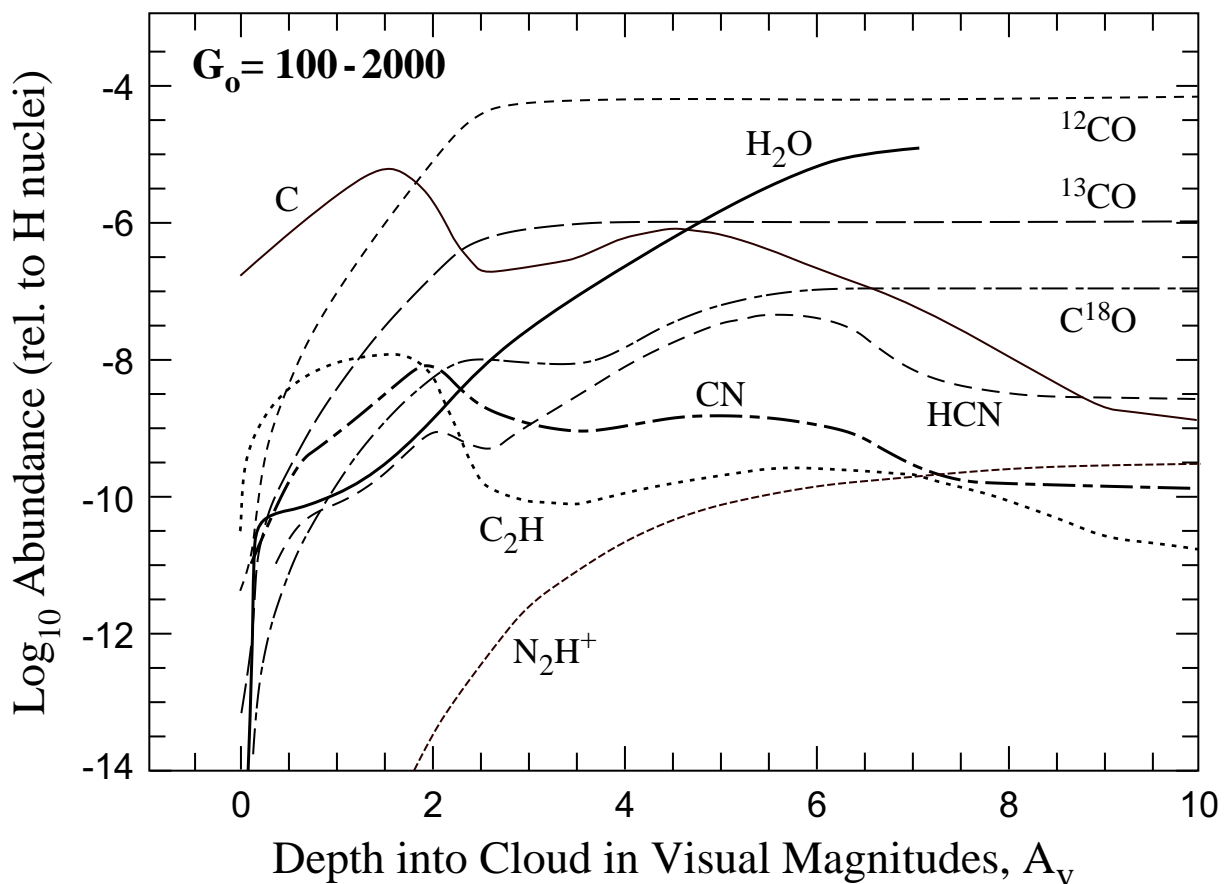
Fig. 15. Predicted abundance profiles for the densities and moderate incident far-ultraviolet field strengths applicable to the extended Orion ridge. Specifically, the CN and HCN profiles are adapted from Boger & Sternberg (2005) who assumed a hydrogen nuclei density, n_H, of 10^4 cm^{-3} and a FUV intensity, G_o, of 2×10^3. The C, C$_2$H and N$_2$H$^+$ profiles are adapted from Morata & Herbst (2008) who assumed $n_H = 2 \times 10^4$ cm^{-3} and $G_o = 100$. The ^{12}CO, ^{13}CO, C^{18}O and H$_2$O profiles were adapted from Jansen et al. (1995a) who assumed $n_H = 10^5$ cm^{-3} and $G_o = 650$.
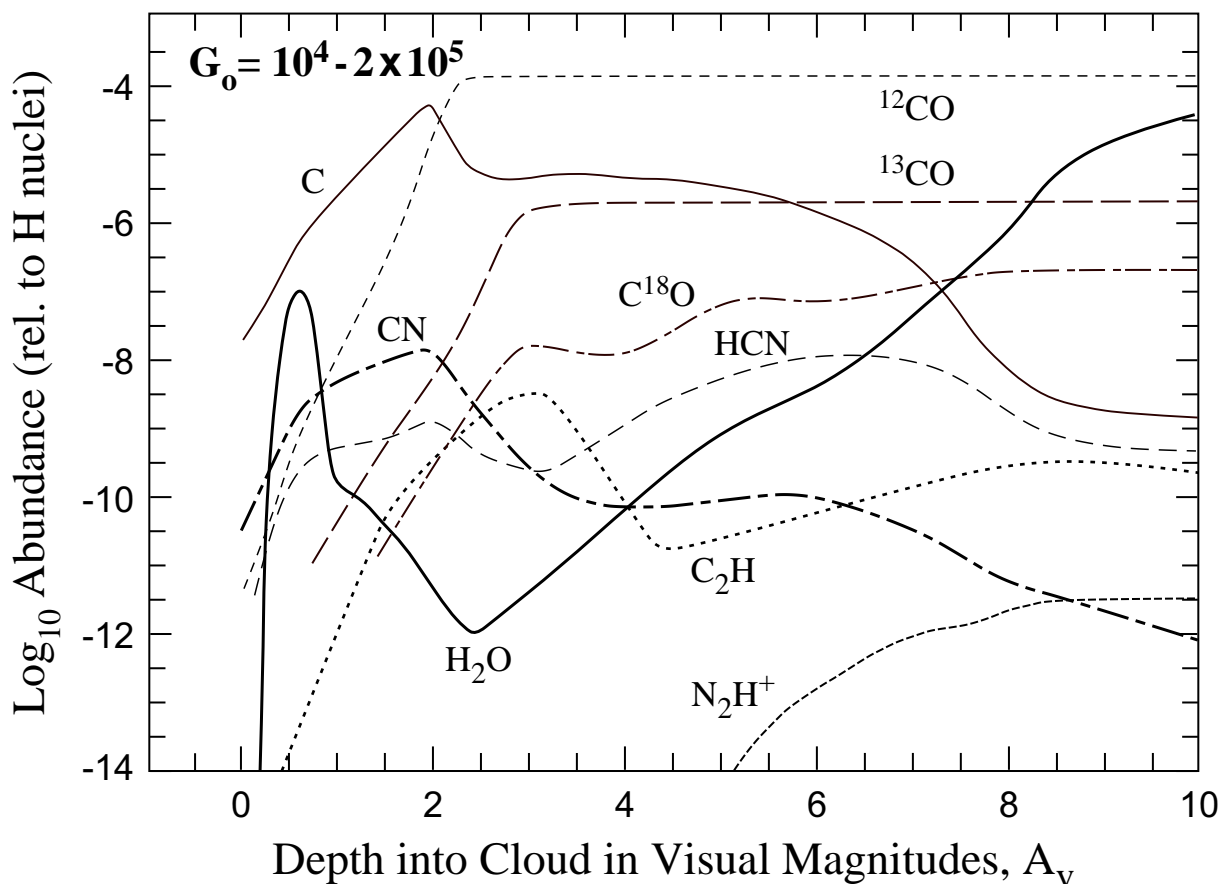
Fig. 16. Predicted abundance profiles for the densities and strong incident far-ultraviolet field strengths applicable to the Orion ridge close to the Trapezium cluster (see text). Specifically, the C, ^{12}CO, CN, and HCN profiles are adapted from Boger & Sternberg (2005) who assumed a hydrogen nuclei density, n_H, of 10^5 cm^{-3}, and a FUV intensity, G_o, of 2×10^4. The C$_2$H profile is adapted from Morata & Herbst (2008) who assumed $n_H = 2 \times 10^4$ cm^{-3} and $G_o = 10^4$. The ^{13}CO and C^{18}O profiles were adapted from Jansen et al. (1995b) who assumed $n_H = 2.5 \times 10^5$ cm^{-3} and $G_o = 4.4 \times 10^4$. The H$_2$O and N$_2$H$^+$ profiles are adapted from Sternberg & Dalgarno (1995) who assumed $n_H = 10^6$ cm^{-3} and $G_o = 2 \times 10^5$.
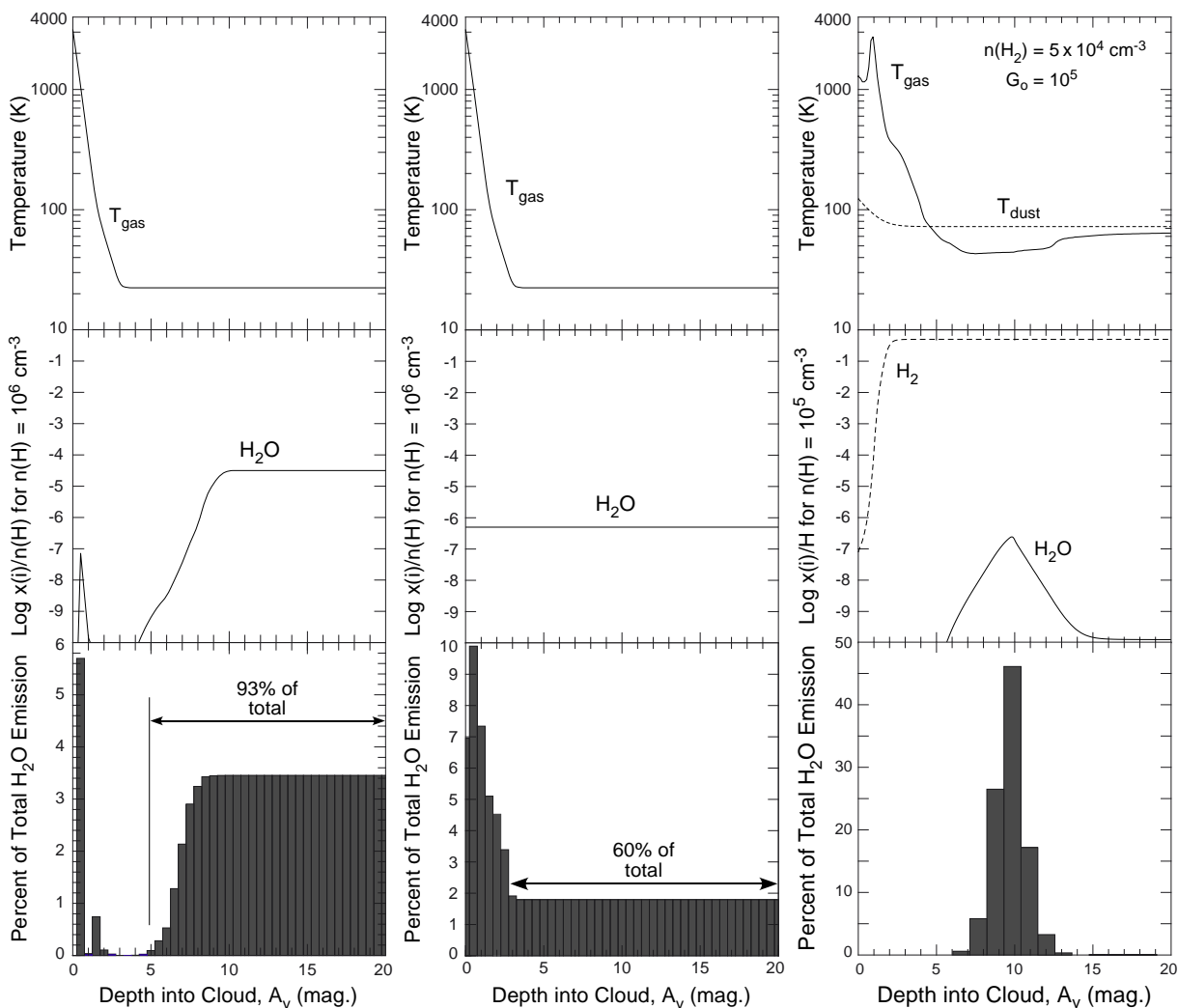
Fig. 17. Calculated fraction of the total H_2O emission arising from various depths into a dense cloud between $A_V = 0$ to 20. *Left panel*: Profiles of temperature and H_2O abundance obtained from Sternberg & Dalgarno (1995) for a PDR with $n(H_2) = 5 \times 10^5$ cm^{-3} and $G_o = 2 \times 10^5$. The profiles in their paper cover the range $0 < A_V < 10$; our calculations were extended to an A_V of 20 by assuming that both the temperature and H_2O abundance at $A_V = 10$ have reached equilibrium values that apply between $A_V = 10$ and 20. *Middle panel*: For the case of a constant water abundance, we use the Sternberg and Dalgarno PDR density and temperature profile, but assume a constant H_2O abundance of 5×10^{-7}, consistent with maximum H_2O abundance predicted by Hollenbach et al. (2009). *Right panel*: Profiles of temperature and H_2O abundance from Hollenbach et al. (2009) model. In all cases, the collisional rates of Faure et al. (2007) were used and ortho-to-para H_2 and H_2O ratios of 3:1 and total line width of 3 km s^{-1} were assumed.
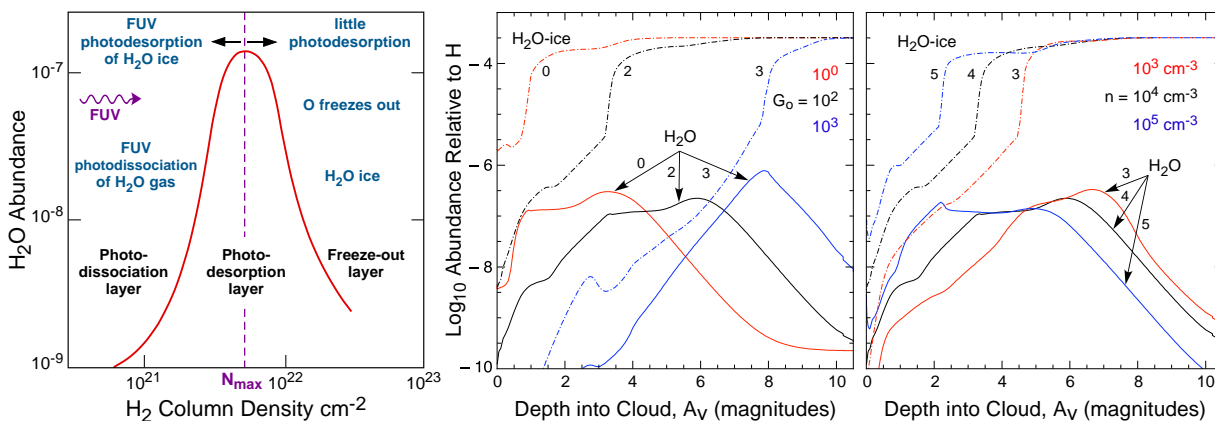
Fig. 18. *Left*: Schematic depiction of water-vapor zone within molecular clouds, including the main processes affecting the gas-phase water abundance. *Center*: H_2O and H_2O-ice abundances for a cloud with $n = 10^4$ cm^{-3} but with a variety of FUV field strengths incident on the cloud surface (after Hollenbach et al. 2009). *Right*: Effect of changing the gas density for the FUV field strength $G_o = 10^2$ where, following the convention used in Hollenbach et al. (2009), n is the gas-phase hydrogen nucleus number density [$\sim n(H) + 2n(H_2 + n(H^+)$]. The Hollenbach et al. (2009) results depict steady state abundance profiles, including CO depletion due to reactions with He^+. Prior to the depletion of CO, the gas-phase H_2O abundances at high A_V will be greater than shown here, though the peak of water abundance at intermediate A_V is likely retained. (see text).

TABLE 1.

Spectral Lines Observed by *SWAS* and *FCRAO*

		SWAS		
Species	Transition	Energy Above Ground State (E_u/k)	Frequency (GHz)	Critical Density (cm^{-3})
O_2	$3,3 - 1,2$	26 K	487.249	10^3
CI	$^3P_1 - {}^3P_0$ [a]	24 K	492.161	10^3
$H_2^{18}O$	$1_{10} - 1_{01}$ [a]	26 K	547.676	8×10^7 [b]
^{13}CO	$J = 5 - 4$	79 K	550.926	2×10^5
$H_2^{16}O$	$1_{10} - 1_{01}$ [a]	27 K	556.936	8×10^7 [b]
		FCRAO		
C_2H	N=1−0, J=$\frac{1}{2} - \frac{1}{2}$	4.20 K	87.402 [c]	2×10^5
HCN	J=1−0	4.25 K	88.632 [c]	2×10^6
N_2H^+	J=1−0	4.47 K	93.174 [c]	2×10^5
$C^{18}O$	J=1−0	5.27 K	109.782	2×10^3
^{13}CO	J=1−0	5.29 K	110.201	2×10^3
CN	N=1−0, J=$\frac{3}{2} - \frac{1}{2}$	5.45 K	113.491 [c]	4×10^4
^{12}CO	J=1−0	5.53 K	115.271	2×10^3

[a] Ground-state transition.

[b] Based on the collisional rates of Dubernet et al. (2006) and Faure et al. (2007) and assuming collisions with ortho- and para-H_2 in the ratio of 0.03, the LTE value at 30 K. The critical density for $H_2^{16}O$ will likely be less than this value due to significant radiation trapping in this line. The critical density for $H_2^{18}O$ could be reduced due to the same effect (see text).

[c] Rest frequency of the strongest hyperfine component.